Pure Appl. Geophys. 176 (2019), 3929–3949

https://doi.org/10.1007/s00024-018-2054-z

Pure and Applied Geophysics

Green's Functions for Post-seismic Strain Changes in a Realistic Earth Model and Their Application to the Tohoku-Oki M_w 9.0 Earthquake

Tai Liu,[1] Guangyu Fu,[2] Yawen She,[3] and Cuiping Zhao[2]

Abstract—Based on a spherically symmetric, self-gravitating viscoelastic Earth model, we derive a complete set of Green's functions for the post-seismic surface strain changes for four independent dislocation sources: strike-slip, dip-slip, and horizontal and vertical tensile point sources. The post-seismic surface strain changes caused by an arbitrary earthquake can be obtained by a combination of the above Green's functions. The post-seismic surface strain changes in the near field agree well with the results calculated by the method in a half-space Earth model (Wang et al. in Comupt Geosci 32:527–541, 2006), which verifies our Green's functions. With an increase in the epicentral distance, the effect of the curvature on both the co- and post-seismic strain changes clearly increases, revealing the importance of our spherical theory for far-field calculations. Next, we use our Green's functions to simulate the post-seismic surface strain changes that were caused by the viscoelastic relaxation of the mantle over the 6-year period after the Tohoku-Oki M_w 9.0 earthquake. Based on continuous Global Positioning System (GPS) observations around Honshu Island of Japan, Northeastern China, South Korea and the Russian Far East, we also deduce the post-seismic strain changes caused by the Tohoku-Oki M_w 9.0 earthquake. Overall, the distributions of the calculated and GPS-derived strain changes agree well each other. Finally, we compare the relative error between the observed and simulated strain changes over the 3.0–4.5-year period after the earthquake in both the near and far field. We find that the relative errors decrease as the epicentral distance increases, which validates our Green's functions for research in the far field.

Key words: Post-seismic strain changes, spherical dislocation theory, Green's functions, preliminary reference Earth model (PREM), Tohoku-Oki M_w 9.0 earthquake.

1. Introduction

Because of developments in modern geodetic techniques, post-seismic deformations caused by large earthquakes can be detected by Global Positioning System (GPS), interferometric synthetic-aperture radar (InSAR) and other measurements. Such data make it possible to study the Earth's internal structure and seismogenic mechanisms. In particular, the GPS provides efficient, stable and accurate results for monitoring of large-scale crustal movements, plays an important role in inversion of fault slip distributions (Ozawa et al. 2011; Zhou et al. 2014) and supplements detection of stress and strain changes (Savage et al. 1986, 2001; Tape et al. 2009). Using geodetic data, the strain changes induced by earthquakes can be continuously monitored (Araya et al. 2010, 2017; Ohzono et al. 2012). Strain is a more direct indicator than displacements to represent deformation (Takahashi 2011). To explain these strain data, theoretical calculations of co- and post-seismic strain changes are necessary.

Scientists have developed dislocation theories to compute co- and post-seismic deformations. Based on a half-space Earth model, Steketee (1958) first introduced dislocation theory into the field of seismology. Since then, many researchers have studied co-seismic deformations caused by earthquakes (Chinnery 1961, 1963; Maruyama 1964). Okada (1985) and Okubo (1991, 1992) presented several sets of concise formulae to calculate co-seismic deformations (gravity, geoid, displacement and strain), which have been widely applied in seismology and geodesy. Fukahata and Matsu'ura (2005, 2006), Hashima et al. (2008, 2014) and Wang et al. (2003, 2006) provided dislocation theories to

[1] Institute of Geophysics, China Earthquake Administration, Beijing 100081, China.
[2] Institute of Earthquake Forecasting, China Earthquake Administration, Beijing 100036, China. E-mail: fugy@cea-ies.ac.cn
[3] Hebei Seismological Bureau, Shijiazhuang 050021, China.

compute the co- and post-seismic strain changes in a multilayered half-space model. Their theories ignore the effect of the curvature of the Earth (Sun and Okubo 2002; Dong et al. 2014, 2016), and the validity of their theories is limited to the near field. Taking the curvature of the Earth into account, Sun et al. (2006, 2009) presented a complete theory to calculate the co-seismic strain changes in a layered spherical model. Takagi and Okubo (2017) and Tang and Sun (2017) presented asymptotic expressions for the co-seismic surface strain changes in a homogeneous Earth model, which improves the efficiency of spherical dislocation theories greatly. However, their methods can only be used to study co-seismic strain changes. They ignore the viscosity structure of the Earth.

Using the normal mode method, Piersanti et al. (1995) solved the post-seismic deformation equations in a spherically symmetrical Earth model. They considered the curvature and the viscosity structure of the Earth but not the issue of compressibility. Pollitz (1997) took into account the compressibility of the Earth, whereas his model consists of limited layers, in which the allowable radial structure of density and gravity in the unperturbed state is limited, viz. $\rho(r)g(r) = \text{const}/r$). To bypass this difficulty following the normal mode method, Tanaka et al. (2006, 2007) used numerical inverse Laplace integration along a rectangular path to obtain the post-seismic gravity, geoid and displacement changes. However, they did not consider the strain changes following an earthquake.

In this paper, we present a new method to calculate the post-seismic surface strain changes in a self-gravitating, compressible and realistically stratified Earth model. In the following section, we explain the theory of displacements provided by Tanaka et al. (2006, 2007), on which our work is based. In Sect. 3, we derive the expressions for the Green's functions for the post-seismic surface strain changes for four independent point sources. In Sect. 4, we verify our method by comparing the surface strain changes induced by particular dislocation sources using our methods and previous theory (Sun et al. 2006; Wang et al. 2006) to confirm the validity of our method. In Sect. 5, we simulate the post-seismic strain changes induced by the Tohoku-Oki M_w 9.0 earthquake. By comparing the simulated strain changes with those derived from GPS observations, we further show the importance of our Green's functions.

2. Basic Theory of Post-seismic Displacements

In this section, we give an outline of the numerical inverse Laplace integration along a rectangular path presented by Tanaka et al. (2006, 2007), a technique that will be further considered when we discuss the post-seismic strain changes. We assume a dislocation model as shown in Fig. 1. Here, n and v are a unit vector normal to the infinitesimal fault surface dS and a unit slip vector, respectively. Axes 1 and 2 are within the horizontal surface, and axis 3 is the vertical axis.

The viscoelastic global deformations caused by an earthquake can be expressed in the same form as the elastic ones provided by Sun et al. (1996). Specifically, we can get the solution for the equivalent elastic medium in the Laplace domain and then obtain the viscoelastic solution by taking the inverse Laplace transform (Lee 1955; Radok 1957). The displacement $\mathbf{u}$, stress tensor $\boldsymbol{\tau}$ and potential ψ are expanded using the vector spherical harmonics in spherical coordinates (r, θ, φ) as follows (Tanaka et al. 2007):

$$\begin{aligned}\boldsymbol{u}(r,\theta,\varphi,t) &= \sum_{n,m}\left[y_1(r,t;n,m)\boldsymbol{R}_n^m(\theta,\varphi) + y_3(r,t;n,m)\boldsymbol{S}_n^m(\theta,\varphi)\right.\\ &\quad \left. + y_1^{\mathrm{T}}(r,t;n,m)\boldsymbol{T}_n^m(\theta,\varphi)\right], \boldsymbol{\tau}(r,\theta,\varphi,t)\cdot\boldsymbol{e}_r\\ &= \sum_{n,m}\left[y_2(r,t;n,m)\boldsymbol{R}_n^m(\theta,\varphi) + y_4(r,t;n,m)\boldsymbol{S}_n^m(\theta,\varphi)\right.\\ &\quad \left. + y_2^{\mathrm{T}}(r,t;n,m)\boldsymbol{T}_n^m(\theta,\varphi)\right],\\ \psi(r,\theta,\varphi,t) &= \sum_{n,m} y_5(r,t;n,m)Y_n^m(\theta,\varphi),\end{aligned} \tag{1}$$

where

$$\boldsymbol{R}_n^m(\theta,\varphi) = \boldsymbol{e}_r Y_n^m(\theta,\varphi), \tag{2}$$

$$\boldsymbol{S}_n^m(\theta,\varphi) = \left[\boldsymbol{e}_\theta\frac{\partial}{\partial\theta} + \boldsymbol{e}_\varphi\frac{1}{\sin\theta}\frac{\partial}{\partial\varphi}\right]Y_n^m(\theta,\varphi), \tag{3}$$

$$\boldsymbol{T}_n^m(\theta,\varphi) = \left[\boldsymbol{e}_\theta\frac{1}{\sin\theta}\frac{\partial}{\partial\varphi} - \boldsymbol{e}_\varphi\frac{\partial}{\partial\theta}\right]Y_n^m(\theta,\varphi), \tag{4}$$

$$Y_n^m(\theta,\varphi) = P_n^m(\cos\theta)\mathrm{e}^{im\varphi}. \tag{5}$$

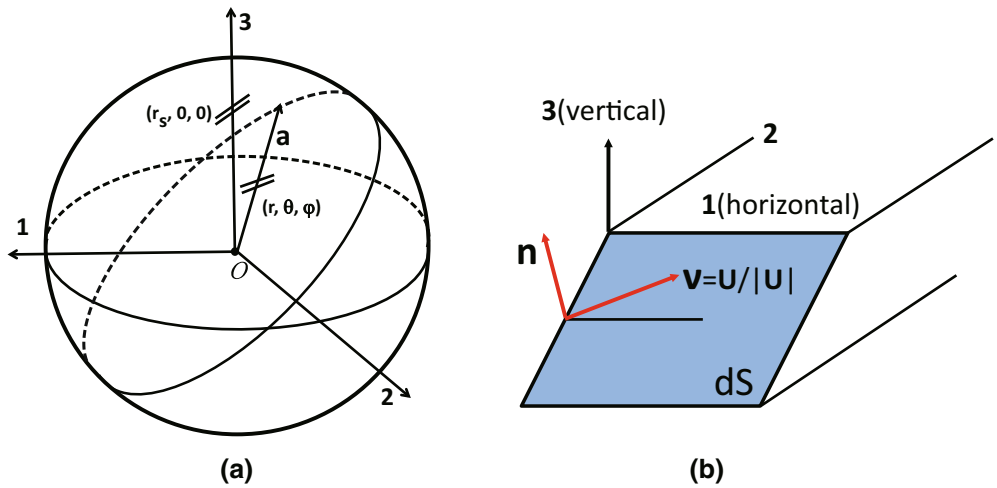

Figure 1
Diagram of the seismic source. Axes 1 and 2 are the two horizontal axes, and axis 3 is the vertical axis. (r_S, 0, 0) is the location of the source. (r, θ, φ) is an arbitrary point. **a** is the radius of the Earth. dS denotes the fault surface with a normal vector n. v is a unit slip vector parallel to U

Herein, (r, θ, φ) and $\boldsymbol{e}_i$ are the conventional polar coordinates and unit base vectors, respectively. $P_n^m(\cos\theta)$ is the unnormalized Legendre's function and $P_n^{-|m|}(\cos\theta) = (-1)^m P_n^{|m|}(\cos\theta)$. $y_1(r, t; n, m)$ and $y_3(r, t; n, m)$ are the radial functions representing the vertical and horizontal displacement, respectively. $y_1^{\mathrm{T}}(r, t; n, m)$ denotes the displacement for the toroidal mode. $y_5(r, t; n, m)$ denotes the potential change. $y_2(r, t; n, m)$ and $y_4(r, t; n, m)$ are the radial functions corresponding to the vertical and horizontal stress, respectively. $y_2^{\mathrm{T}}(r, t; n, m)$ denotes the stress for the toroidal mode. An additional $y_6(r, t; n, m)$ function is introduced for mathematical convenience.

The solution for a Maxwell solid in the Laplace domain in an equivalent elastic medium can be found in Peltier (1974), and the apparent elastic deformation with a Laplace variable s satisfies the following differential equations:

$$\frac{\mathrm{d}\tilde{y}_i(r,s;n,m)}{\mathrm{d}r} = \sum_j A_{i,j}(r,s;n)\tilde{y}_j(r,s;n,m) + \tilde{S}_i(s;n,m), \quad (6)$$

$$\frac{\mathrm{d}\tilde{y}_i^{\mathrm{T}}(r,s;n,m)}{\mathrm{d}r} = \sum_j B_{i,j}(r,s;n)\tilde{y}_j^{\mathrm{T}}(r,s;n,m) + \tilde{S}_i^{\mathrm{T}}(s;n,m), \quad (7)$$

where explicit expressions for the homogeneous terms are given by Takeuchi and Saito (1972) and are listed in Appendix 1. The inhomogeneous terms

$$\tilde{S}_i = \tilde{y}_i(r_{\mathrm{s}} + 0, s; n, m) - \tilde{y}_i(r_{\mathrm{s}} - 0, s; n, m), \quad (8)$$

$$\tilde{S}_i^{\mathrm{T}} = \tilde{y}_i^{\mathrm{T}}(r_{\mathrm{s}} + 0, s; n, m) - \tilde{y}_i^{\mathrm{T}}(r_{\mathrm{s}} - 0, s; n, m) \quad (9)$$

are the source functions with a point dislocation at $r = r_{\mathrm{s}}$ (Saito 1967; Takeuchi and Saito 1972), and the boundary condition on the free surface is

$$\tilde{y}_2(a) = \tilde{y}_4(a) = \tilde{y}_6(a) = \tilde{y}_2^{\mathrm{T}}(a) = 0. \quad (10)$$

We can obtain the solutions $\tilde{y}_i(r, s; n, m)$ and $\tilde{y}_i^{\mathrm{T}}(r, \mathrm{s}; n, m)$ for the equivalent elastic problem by solving Eqs. (6) and (7). The viscoelastic solution in the time domain can be obtained by taking the inverse Laplace transform of these equations. However, it is not feasible to obtain the solutions directly when innumerable layers and compressibility are considered simultaneously (Fang and Hager 1994; Piersanti et al. 1995; Vermeersen and Sabadini 1997; Wang 1999). It is extremely difficult to obtain the solutions for the y-variables by summing the normal modes of all the poles in the Laplace domain. This is because the normal mode method cannot evaluate an infinite set of poles when compressibility and continuous radial structures are considered. Tanaka et al.

(2006, 2007) carried out the numerical inverse Laplace integration on a closed path to include all poles, which evaluates the contributions from all the eigenmodes and avoids the intrinsic numerical difficulties of previous theories. Inverting the Laplace integration in Eqs. (11, 12), we obtain expressions for the y-variables $y_i(r, t; n, m)$ and $y_i^{\mathrm{T}}(r, t; n, m)$ (Eqs. 13–20).

$$y_i(r,t;n,m) = \frac{1}{2\pi i}\oint \tilde{y}_i(r,s;n,m)\frac{e^{st}}{s}\mathrm{d}s, \tag{11}$$

$$y_i^{\mathrm{T}}(r,t;n,m) = \frac{1}{2\pi i}\oint \tilde{y}_i^{\mathrm{T}}(r,s;n,m)\frac{e^{st}}{s}\mathrm{d}s, \tag{12}$$

Finally, we obtain the expressions for the post-seismic displacements by substituting Eqs. (13–20) into Eq. (1):

$$\begin{aligned} y_1(a,t;n,0) = &\left[(n_1v_1+n_2v_2)F_u^1(t;n)\right. \\ &\left.+n_3v_3F_u^2(t;n)\right]U\,\mathrm{d}S, \end{aligned} \tag{13}$$

$$\begin{aligned} y_1(a,t;n,\pm1) = &[\pm(n_3v_1+n_1v_3) \\ &-i(n_2v_3+n_3v_2)]F_u^3(t;n)U\,\mathrm{d}S, \end{aligned} \tag{14}$$

$$\begin{aligned} y_1(a,t;n,\pm2) = &[(-n_1v_1+n_2v_2) \\ &\pm i(n_1v_2+n_2v_1)]F_u^4(t;n)U\,\mathrm{d}S, \end{aligned} \tag{15}$$

$$\begin{aligned} y_3(a,t;n,0) = &\left[(n_1v_1+n_2v_2)F_{\mathrm{v}}^1(t;n)\right. \\ &\left.+n_3v_3F_v^2(t;n)\right]U\,\mathrm{d}S, \end{aligned} \tag{16}$$

$$\begin{aligned} y_3(a,t;n,\pm1) = &[\pm(n_3v_1+n_1v_3) \\ &-i(n_2v_3+n_3v_2)]F_v^3(t;n)U\,\mathrm{d}S, \end{aligned} \tag{17}$$

$$\begin{aligned} y_3(a,t;n,\pm2) = &[(-n_1v_1+n_2v_2) \\ &\pm i(n_1v_2+n_2v_1)]F_v^4(t;n)U\,\mathrm{d}S, \end{aligned} \tag{18}$$

$$\begin{aligned} y_1^{\mathrm{T}}(a,t;n,\pm1) = &[\pm(n_2v_3+n_3v_2) \\ &-i(n_3v_1+n_1v_3)]F_t^1(t;n)U\,\mathrm{d}S, \end{aligned} \tag{19}$$

$$\begin{aligned} y_1^{\mathrm{T}}(a,t;n,\pm2) = &[(n_1v_2+n_2v_1) \\ &\pm i(n_1v_1-n_2v_2)]F_t^2(t;n)U\,\mathrm{d}S. \end{aligned} \tag{20}$$

The expressions for F_v^i $(i = 1,\ldots,4)$, F_u^i $(i = 1,\ldots,4)$ and F_t^i $(i = 1, 2)$ can be found in Appendix 2.

3. Green's Functions for Post-seismic Strain Changes

Sun et al. (2006) presented a set of Green's functions for co-seismic strain changes in a spherically symmetric Earth model. Here, we derive a set of Green's functions for the post-seismic strain changes based on the same Earth model. According to the conventional theory of elasticity, we express the components of the strain tensor in terms of the displacements as follows (Takeuchi and Saito 1972):

$$\begin{aligned} e_{rr} &= \frac{\partial u_r}{\partial r}, \\ e_{\theta\theta} &= \frac{1}{r}\frac{\partial u_\theta}{\partial\theta}+\frac{1}{r}u_r, \\ e_{\varphi\varphi} &= \frac{1}{r\sin\theta}\frac{\partial u_\varphi}{\partial\varphi}+\frac{1}{r}u_\theta\cot\theta+\frac{1}{r}u_r, \\ e_{\theta\varphi} &= \frac{1}{r}\frac{\partial u_\varphi}{\partial\theta}-\frac{1}{r}u_\varphi\cot\theta+\frac{1}{r\sin\theta}\frac{\partial u_\theta}{\partial\varphi}, \\ e_{r\theta} &= \frac{\partial u_\theta}{\partial r}-\frac{1}{r}u_\theta+\frac{1}{r}\frac{\partial u_r}{\partial\theta}, \\ e_{r\varphi} &= \frac{1}{r\sin\theta}\frac{\partial u_r}{\partial\varphi}+\frac{\partial u_\varphi}{\partial r}-\frac{1}{r}u_\varphi. \end{aligned} \tag{21}$$

After inserting the displacement components that were defined in Sect. 2 into Eq. (21), we obtain the strain components in Eqs. (22–45). Because the last two components $e_{r\theta}$ and $e_{r\varphi}$ vanish on the Earth's free surface, the total strain change on the Earth's surface can be completely represented by the remaining four strain components.

The strain changes in vertical direction e_{rr} can be expressed as

$$\begin{aligned} e_{rr}(a,\theta,\varphi,t) = &\{(n_1v_1+n_2v_2)G_{rr}^1(\theta,t)+n_3v_3G_{rr}^2(\theta,t) \\ &+\left[(n_1v_3+n_3v_1)\cos\varphi\right. \\ &\left.+(n_2v_3+n_3v_2)\sin\varphi\right]G_{rr}^3(\theta,t) \\ &+\left[(n_1v_1-n_2v_2)\cos2\varphi\right. \\ &\left.+(n_1v_2+n_2v_1)\sin2\varphi\right]G_{rr}^4(\theta,t)\}\frac{U\mathrm{d}S}{a^3}. \end{aligned} \tag{22}$$

Herein, $G^i_{rr}(\theta,t)$ (i = 1,…,4) denotes the Green's function for strain changes in vertical direction. a = 6371 km, U is the magnitude of the dislocation. dS denotes the area of the dislocation.

$$G^1_{rr}(\theta,t)=\frac{\lambda}{\lambda+2\mu}\sum_{n=0}^{\infty}\left[-2a^2F^1_u(t;n)+n(n+1)a^2F^1_v(t;n)\right]P^0_n(\cos\theta), \tag{23}$$

$$G^2_{rr}(\theta,t)=\frac{\lambda}{\lambda+2\mu}\sum_{n=0}^{\infty}\left[-2a^2F^2_u(t;n)+n(n+1)a^2F^2_v(t;n)\right]P^0_n(\cos\theta), \tag{24}$$

$$G^3_{rr}(\theta,t)=\frac{\lambda}{\lambda+2\mu}\sum_{n=1}^{\infty}\left[-4a^2F^3_u(t;n)+n(n+1)a^2F^3_v(t;n)\right]P^1_n(\cos\theta), \tag{25}$$

$$G^4_{rr}(\theta,t)=\frac{\lambda}{\lambda+2\mu}\sum_{n=2}^{\infty}\left[-4a^2F^4_u(t;n)+n(n+1)a^2F^4_v(t;n)\right]P^2_n(\cos\theta). \tag{26}$$

The expressions for F^i_v (i = 1,…,4) and F^i_u (i = 1,…,4) can be found in Appendix 2.

Similarly, the Green's functions for strain changes in horizontal direction, viz. $G^i_{\theta\theta}(\theta,t), G^i_{\varphi\varphi}(\theta,t)$, $G^i_{\theta\varphi}(\theta,t)$, ($i$ = 1,…,4), can be expressed as follows:

$$\begin{aligned}e_{\theta\theta}(a,\theta,\varphi,t)=\{&(n_1v_1+n_2v_2)G^1_{\theta\theta}(\theta,t)+n_3v_3G^2_{\theta\theta}(\theta,t)\\&+\left[(n_1v_3+n_3v_1)\cos\varphi\right.\\&+\left.(n_2v_3+n_3v_2)\sin\varphi\right]G^3_{\theta\theta}(\theta,t)\\&+\left[(n_1v_1-n_2v_2)\cos2\varphi\right.\\&+\left.(n_1v_2+n_2v_1)\sin2\varphi\right]G^4_{\theta\theta}(\theta,t)\\&+\left[-(n_2v_3+n_3v_2)\sin\varphi\right.\\&+\left.(n_1v_3+n_3v_1)\cos\varphi\right]G^{t1}_{\theta\theta}(\theta,t)\\&+\left[(n_1v_2+n_2v_1)\sin2\varphi\right.\\&+\left.(n_1v_1+n_2v_2)\cos2\varphi\right]G^{t2}_{\theta\theta}(\theta,t)\}\frac{U\mathrm{d}S}{a^3}.\end{aligned} \tag{27}$$

Herein,

$$G^1_{\theta\theta}(\theta,t)=\sum_{n=0}^{\infty}\left[a^2F^1_u(t;n)P^0_n(\cos\theta)+a^2F^1_v(t;n)\frac{\mathrm{d}^2P^0_n(\cos\theta)}{\mathrm{d}\theta^2}\right], \tag{28}$$

$$G^2_{\theta\theta}(\theta,t)=\sum_{n=0}^{\infty}\left[a^2F^2_u(t;n)P^0_n(\cos\theta)+a^2F^2_v(t;n)\frac{\mathrm{d}^2P^0_n(\cos\theta)}{\mathrm{d}\theta^2}\right], \tag{29}$$

$$G^3_{\theta\theta}(\theta,t)=\sum_{n=1}^{\infty}\left[2a^2F^3_u(t;n)P^0_n(\cos\theta)+2a^2F^3_v(t;n)\frac{\mathrm{d}^2P^1_n(\cos\theta)}{\mathrm{d}\theta^2}\right], \tag{30}$$

$$G^4_{\theta\theta}(\theta,t)=\sum_{n=2}^{\infty}\left[2a^2F^4_u(t;n)P^0_n(\cos\theta)+2a^2F^4_v(t;n)\frac{\mathrm{d}^2P^2_n(\cos\theta)}{\mathrm{d}\theta^2}\right], \tag{31}$$

$$G^{t1}_{\theta\theta}(\theta,t)=\sum_{n=1}^{\infty}2a^2F^1_t(t;n)\left[\frac{1}{\sin\theta}\frac{\mathrm{d}P^1_n(\cos\theta)}{\mathrm{d}\theta}-\frac{\cos\theta}{\sin^2\theta}P^1_n(\cos\theta)\right], \tag{32}$$

$$G^{t2}_{\theta\theta}(\theta,t)=\sum_{n=2}^{\infty}4a^2F^2_t(t;n)\left[\frac{1}{\sin\theta}\frac{\mathrm{d}P^2_n(\cos\theta)}{\mathrm{d}\theta}-\frac{\cos\theta}{\sin^2\theta}P^2_n(\cos\theta)\right]. \tag{33}$$

The expressions for F^i_t (i = 1, 2) can be found in Appendix 2.

Again,

$$\begin{aligned}e_{\varphi\varphi}(a,\theta,\varphi,t)=\{&(n_1v_1+n_2v_2).G^1_{\varphi\varphi}(\theta,t)+n_3v_3G^2_{\varphi\varphi}(\theta,t)\\&+\left[(n_1v_3+n_3v_1)\cos\varphi\right.\\&+\left.(n_2v_3+n_3v_2)\sin\varphi\right]G^3_{\varphi\varphi}(\theta,t)\\&+\left[(n_1v_1-n_2v_2)\cos2\varphi\right.\\&+\left.(n_1v_2+n_2v_1)\sin2\varphi\right]G^4_{\varphi\varphi}(\theta,t)\\&+\left[-(n_2v_3+n_3v_2)\sin\varphi\right.\\&+\left.(n_3v_1+n_1v_3)\cos\varphi\right]G^{t1}_{\varphi\varphi}(\theta,t)\\&+\left[(n_1v_2+n_2v_1)\sin2\varphi\right.\\&+\left.(n_1v_1+n_2v_2)\cos2\varphi\right]G^{t2}_{\varphi\varphi}(\theta,t)\}\frac{U\mathrm{d}S}{a^3}.\end{aligned} \tag{34}$$

Herein,

$$G^1_{\varphi\varphi}(\theta,t)=\sum_{n=0}^{\infty}\left[a^2F^1_u(t;n)P^0_n(\cos\theta)+a^2F^1_v(t;n)\cot\theta\frac{\mathrm{d}P^0_n(\cos\theta)}{\mathrm{d}\theta}\right], \tag{35}$$

$$G^2_{\varphi\varphi}(\theta,t)=\sum_{n=0}^{\infty}\left[a^2F^2_u(t;n)P^0_n(\cos\theta)+a^2F^2_v(t;n)\cot\theta\frac{\mathrm{d}P^0_n(\cos\theta)}{\mathrm{d}\theta}\right], \tag{36}$$

$$G^3_{\varphi\varphi}(\theta,t)=\sum_{n=1}^{\infty}\left[2a^2F^3_u(t;n)P^1_n(\cos\theta)+2a^2F^3_v(t;n)\cot\theta\frac{\mathrm{d}P^1_n(\cos\theta)}{\mathrm{d}\theta}\right], \tag{37}$$

$$G^4_{\varphi\varphi}(\theta,t)=\sum_{n=2}^{\infty}\left[2a^2F^4_u(t;n)P^2_n(\cos\theta)+2a^2F^4_v(t;n)\cot\theta\frac{\mathrm{d}P^2_n(\cos\theta)}{\mathrm{d}\theta}\right], \tag{38}$$

$$G^{t1}_{\varphi\varphi}(\theta,t)=\sum_{n=1}^{\infty}\frac{2a^2F^1_t(t;n)}{\sin\theta}\left[\cot\theta P^1_n(\cos\theta)-\frac{\mathrm{d}P^1_n(\cos\theta)}{\mathrm{d}\theta}\right], \tag{39}$$

$$G^{t2}_{\varphi\varphi}(\theta,t)=\sum_{n=2}^{\infty}\frac{4a^2F^2_t(t;n)}{\sin\theta}\left[\cot\theta P^2_n(\cos\theta)-\frac{\mathrm{d}P^2_n(\cos\theta)}{\mathrm{d}\theta}\right], \tag{40}$$

and

$$\begin{aligned}e_{\theta\varphi}(a,\theta,\varphi,t)&=\{[-(n_1v_3+n_3v_1)\sin\varphi+(n_2v_3+n_3v_2)\cos\varphi]G^1_{\theta\varphi}(\theta,t)\\&+[-(n_1v_1+n_2v_2)\sin2\varphi+(n_1v_2+n_2v_1)\cos2\varphi]G^2_{\theta\varphi}(\theta,t)\\&-[(n_2v_3+n_3v_2)\cos\varphi+(n_3v_1-n_1v_3)\sin\varphi]G^{t1}_{\theta\varphi}(\theta,t)\\&+[(n_1v_2+n_2v_1)\cos2\varphi-(n_1v_1-n_2v_2)\sin2\varphi]G^{t2}_{\theta\varphi}(\theta,t)\}\\&\times\frac{U\mathrm{d}S}{a^3}.\end{aligned} \tag{41}$$

Herein,

$$G^1_{\theta\varphi}(\theta,t)=\sum_{n=1}^{\infty}\frac{4a^2F^3_v(t;n)}{\sin\theta}\left[\frac{\mathrm{d}P^1_n(\cos\theta)}{\mathrm{d}\theta}-\cot\theta P^1_n(\cos\theta)\right], \tag{42}$$

$$G^2_{\theta\varphi}(\theta,t)=\sum_{n=2}^{\infty}\frac{8a^2F^4_v(t;n)}{\sin\theta}\left[\frac{\mathrm{d}P^2_n(\cos\theta)}{\mathrm{d}\theta}-\cot\theta P^2_n(\cos\theta)\right], \tag{43}$$

$$G^{t1}_{\theta\varphi}(\theta,t)=\sum_{n=1}^{\infty}2a^2F^1_t(t;n)\left[\frac{P^1_n(\cos\theta)}{\sin^2\theta}-\cot\theta\frac{\mathrm{d}P^1_n(\cos\theta)}{\mathrm{d}\theta}+\frac{\mathrm{d}^2P^1_n(\cos\theta)}{\mathrm{d}\theta^2}\right], \tag{44}$$

$$G^{t2}_{\theta\varphi}(\theta,t)=\sum_{n=2}^{\infty}2a^2F^2_t(t;n)\left[\frac{P^2_n(\cos\theta)}{\sin^2\theta}-\cot\theta\frac{\mathrm{d}P^2_n(\cos\theta)}{\mathrm{d}\theta}+\frac{\mathrm{d}^2P^2_n(\cos\theta)}{\mathrm{d}\theta^2}\right]. \tag{45}$$

In the equations above, the expressions for F^i_v (i = 1,…,4), F^i_u (i = 1,…,4) and F^i_t (i = 1,2) are given in Appendix 2 and can also be found in Tanaka et al. (2006, 2007). We can calculate the four components of the strain changes excited by an arbitrary shear and tensile dislocation using the above Eqs. (22–45). The physical meaning of $G^i_{rr,\theta\theta,\varphi\varphi,\theta\varphi}$ (i = 1,…,4) is related to the geometry of the four independent point sources (n_i, v_i) that are shown in Table 1. In particular, for the vertical tensile case, the expressions for strain have both phi-independent (isotropic) and phi-dependent terms. The phi-dependent term can be expressed by a vertical strike-slip source (Tanaka et al. 2006; 2007), but we display only the isotropic component of the vertical tensile source in Table 1 to avoid redundant definitions.

4. Characteristics of the Green's Functions for Post-seismic Strain Changes

4.1. Behaviour of the Green's Functions for Post-seismic Strain Changes

The Green's functions for the strain change are a function of source depth, source distance and the time passed since the earthquake. In this section, we compute the strain Green's functions for the strain change for the four independent sources in Table 1. We use the PREM (Dziewonski and Anderson 1981) as an Earth model for the density and the elastic constants (Fig. 2). We assume the thickness of the elastic lithosphere and the viscosity of the mantle to be 40 km and 1×10^{19} Pa s, respectively. Figure 3 shows the time variation in the strain Green's functions component $G_{\varphi\varphi}(\theta, t)$ for a source depth (D_s) of 32 km, at $t = 0+$ year (immediately after an event), 2, 4, 6, 8 and 10 years. The magnitude of the deformations is normalized using $U\mathrm{d}S = a^2$, which is the same operation as carried out by Sun et al. (2006).

Table 1

Relationship between Green's functions (e_{rr}, $e_{\theta\theta}$, $e_{\varphi\varphi}$, $e_{\theta\varphi}$) of strain changes and geometry of point sources

Green's function	(n_1, n_2, n_3) (v_1, v_2, v_3)	Dislocation type
$G^1_{rr}(\theta,t)$ $G^1_{\theta\theta}(\theta,t)$ $G^1_{\varphi\varphi}(\theta,t)$ 0	(1, 0, 0) (1, 0, 0)	Isotropic component of vertical tensile
$G^2_{rr}(\theta,t)$ $G^2_{\theta\theta}(\theta,t)$ $G^2_{\varphi\varphi}(\theta,t)$ 0	(1, 0, 0) (1, 0, 0)	Horizontal tensile
$G^3_{rr}(\theta,t)\ \cos\varphi$ $\left[G^3_{\theta\theta}(\theta,t)+G^{t1}_{\theta\theta}(\theta,t)\right]\cos\varphi$ $\left[G^3_{\varphi\varphi}(\theta,t)+G^{t1}_{\varphi\varphi}(\theta,t)\right]\cos\varphi$ $-\left[G^1_{\theta\varphi}(\theta,t)+G^{t1}_{\theta\varphi}(\theta,t)\right]\sin\varphi$	(1, 0, 0) (1, 0, 0)	Vertical dip-slip
$G^4_{rr}(\theta,t)\ \sin 2\varphi$ $\left[G^4_{\theta\theta}(\theta,t)+G^{t2}_{\theta\theta}(\theta,t)\right]\sin 2\varphi$ $\left[G^4_{\varphi\varphi}(\theta,t)+G^{t2}_{\varphi\varphi}(\theta,t)\right]\sin 2\varphi$ $-\left[G^2_{\theta\varphi}(\theta,t)+G^{t2}_{\theta\varphi}(\theta,t)\right]\cos 2\varphi$	(1, 0, 0) (0, 1, 0)	Vertical strike-slip

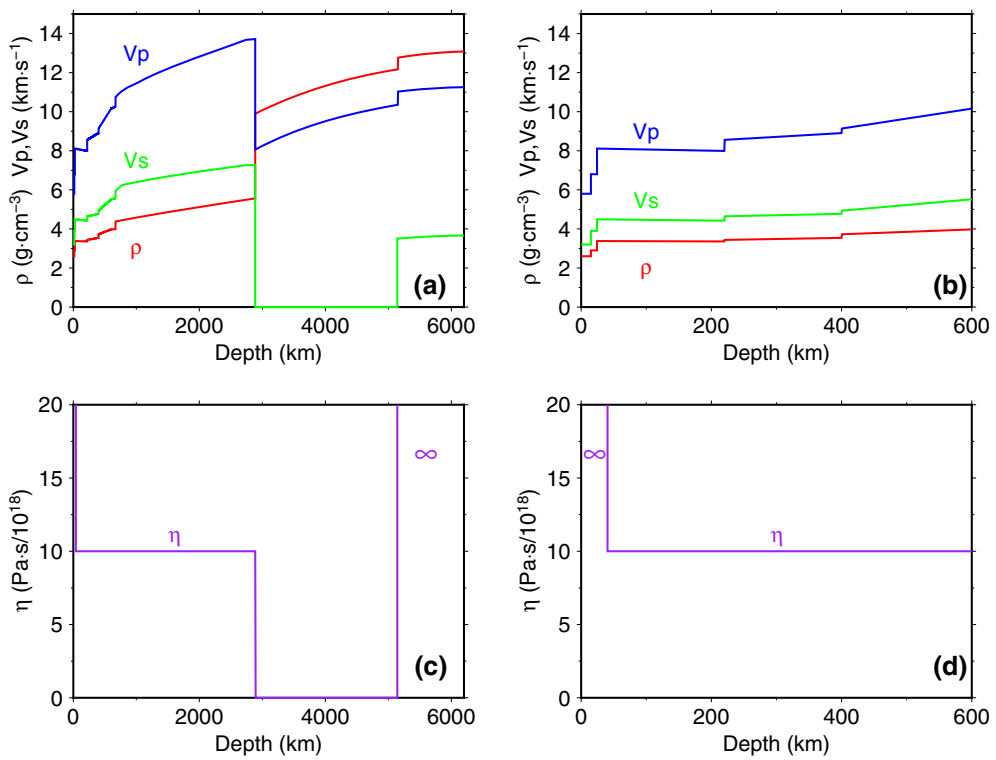

Figure 2

Viscoelastic Earth model used to compute the strain Green's functions. Density ρ and *P*- and *S*-wave velocities are shown in **a** and **b**, respectively. The viscosity profiles are shown in **c**, **d**. The viscosity is infinite at a depth of 0–40 km and in the inner core. The shallower part of the profile is magnified and shown in **b**, **d**

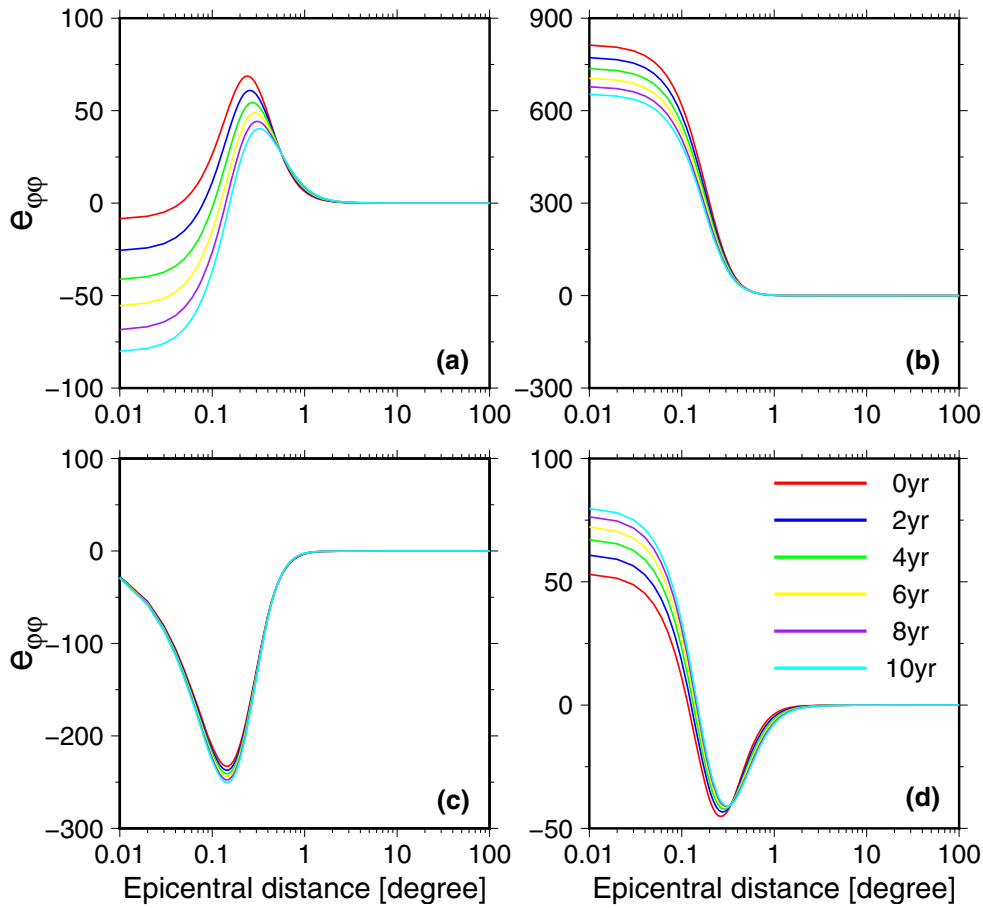

Figure 3
Strain component of $e_{\varphi\varphi}$ for four sources in Table 1. **a** Isotropic component of vertical tensile, **b** horizontal tensile, **c** vertical dip-slip, **d** vertical strike-slip. The results are normalized using $Uds = a^2$

The strain Green's functions in Fig. 3 show a similar tendency in the time domain to those of the displacements in Tanaka et al. (2006, 2007). The shorter the time since earthquake occurrence, the closer the post-seismic Green's function is to the co-seismic Green's function. As the time elapsed after the earthquake increases, the Green's functions increase with the same trend of convergence. This reflects the consistency and gradual change of the co- and post-seismic Green's functions (Gao et al. 2017). Assembling the strain Green's functions for the four independent seismic sources mentioned above, we can calculate the post-seismic strain changes raised by an arbitrary point source.

4.2. *Verification of the Green's Functions for Post-seismic Strain Changes*

To prove the validity of our results, we compare our results with those of Sun et al. (2006) and Wang et al. (2006), which are based on the same layered Earth model (Fig. 2). For simplicity, we study the co- and post-seismic strain changes caused by a point event with a dip-slip angle of 45° and a seismic depth of 10 km. In this case, n and v are $\left(-\frac{1}{\sqrt{2}}, 0, \frac{1}{\sqrt{2}}\right)\left(\frac{1}{\sqrt{2}}, 0, \frac{1}{\sqrt{2}}\right)$, respectively, and the strain components $e_{\varphi\varphi}(\theta, t)$ in Eq. (34) can be written as $-\frac{1}{2}G^1_{\varphi\varphi}(\theta,t) + \frac{1}{2}G^2_{\varphi\varphi}(\theta,t) - \frac{1}{2}G^4_{\varphi\varphi}(\theta,t)\cos(2\varphi)$. As an example, we calculate the co-seismic strain changes in the $e_{\varphi\varphi}$ direction ($\varphi = 0°$) caused by a simple point event using the above three methods

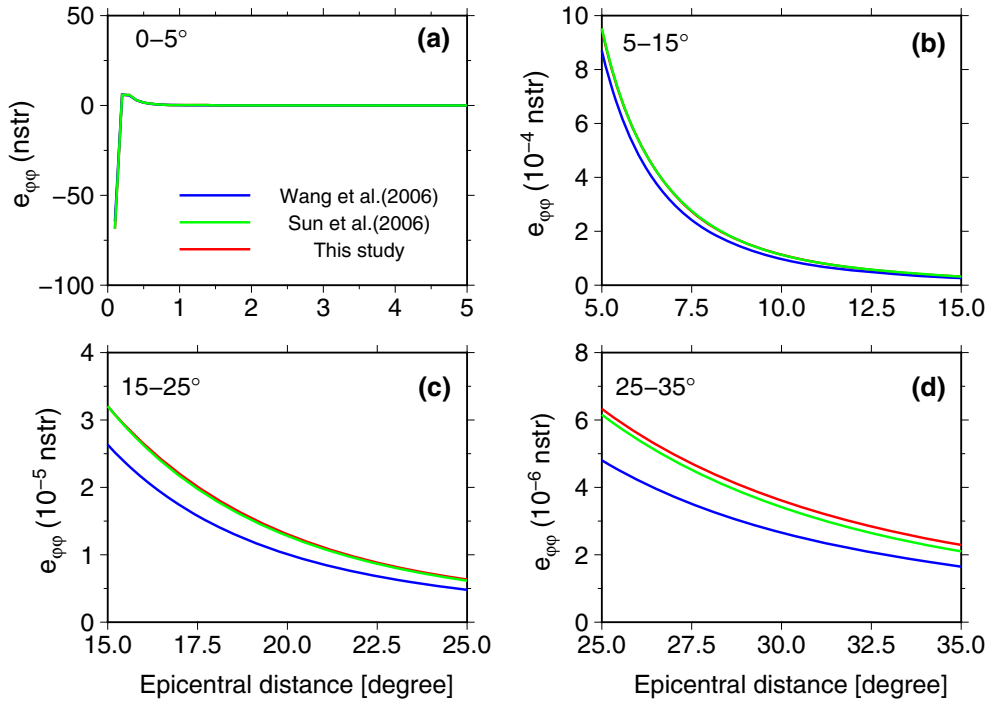

Figure 4
Comparison of our co-seismic strain changes in $e_{\varphi\varphi}$ direction ($\varphi = 0°$) caused by a point event (a dip-slip angle of 45° and a depth of 10 km) with those calculated by Sun et al. (2006) and Wang et al. (2006). **a**–**d** the results in the four epicentral intervals: 0–5°, 5–15°, 15–25° and 25–35°, respectively

(Fig. 4), using the same layered Earth model as that shown in Fig. 2. The magnitude of the deformations is normalized using $U\mathrm{d}S = 1\ \mathrm{m} \times (1\ \mathrm{km})^2$. The blue, green and red lines denote the co-seismic strain change results obtained from the half-space dislocation theory of Wang et al. (2006), the spherical dislocation theory of Sun et al. (2006) and the method presented in this study. We find excellent agreement between the results of Sun et al. (2006) and our method in both the near and far fields, which verifies the validity of our results for the co-seismic responses. However, the agreement between the results of Wang et al. (2006) and ours is limited to the near field. The differences between our results and theirs reach 17.8% for epicentral distance larger than 15°. This reflects the curvature effect.

Next, we examine the viscoelastic responses of our method with the same operation. We calculate the post-seismic strain changes a period of 100 years after a dip-slip event using the method of Wang et al. (2006) and our method. To show the overall trend in the two sets of results, we display the time-dependent variation in the post-seismic strain changes at four epicentral distances (5°, 15°, 25° and 35°) in Fig. 5. We find that the results have similar relaxation characteristics, and the differences between the post-seismic strain change results in the far field are more obvious than those in the near field, which indicates the necessity of using spherical dislocation theory for studying the viscoelastic relaxation in the far field. The relaxation characteristics of the two sets of results are similar, especially in the near field (Fig. 5a), which again verifies our method.

Next, we display the effect of the curvature at each of the epicentral distances shown in Fig. 6, which was calculated using the following equation:

$$\varepsilon = \frac{|e_{\mathrm{s}} - e_{\mathrm{h}}|}{|e_{\mathrm{s}}|}. \tag{46}$$

Herein, e_{s} denotes the strain change corresponding to a spherical model (in this study), and e_{h} denotes the strain change corresponding to the half-space model used by Wang et al. (2006). Figure 6 shows the rapid

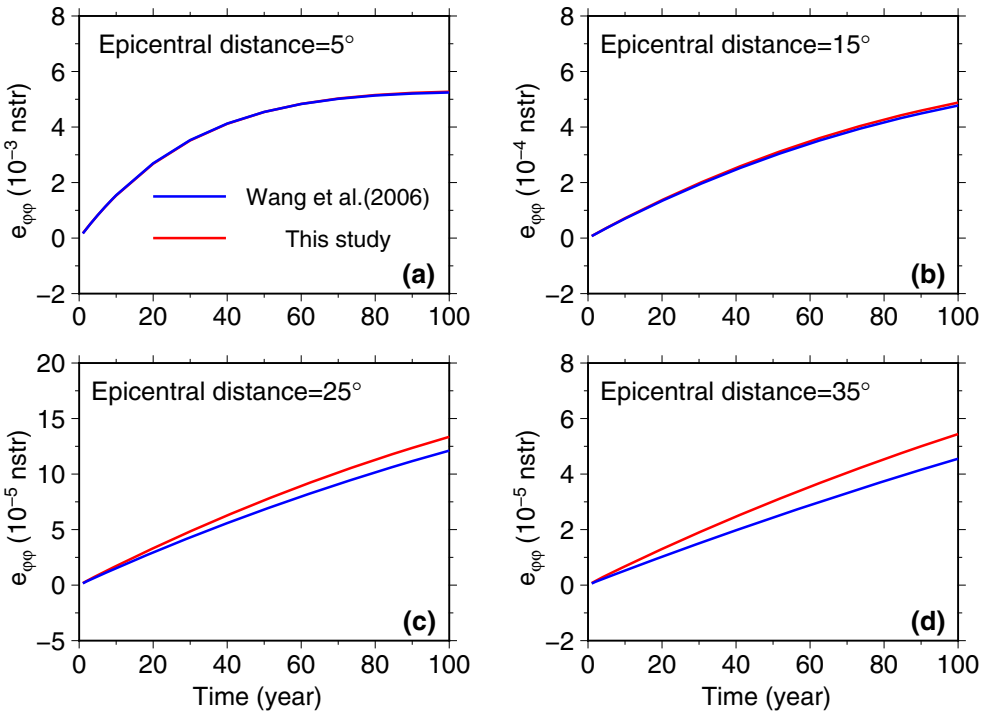

Figure 5
Comparison of our post-seismic strain changes caused by a point event (a dip-slip angle of 45° and a seismic depth of 10 km) with those obtained using the half-space theory of Wang et al. (2006). The post-seismic strain changes from 1 to 100 years after the seismic event. **a**–**d** The results at four epicentral distances: 5°, 15°, 25° and 35°, respectively

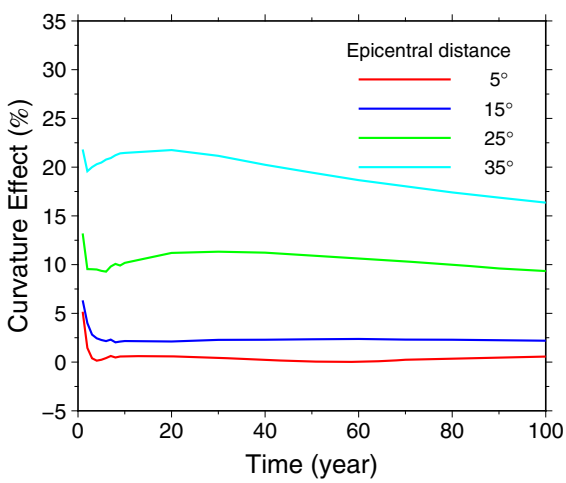

Figure 6
Time-dependent variation in the curvature effect at each epicentral distance. Red, blue, green and cyan lines show the results at four epicentral distances: 5°, 15°, 25° and 35°, respectively

increase in the curvature effect at an epicentral distance larger than 15°, while the effect is less than 5% as a whole for distance smaller than 15°.

Assuming an epicentral distance of 15°, we study the effect of curvature over the first 10,000 years after the seismic event and show the results in Fig. 7. The effect of curvature is approximately 6.9% about 1 year after the event, and then it becomes as small as 2.0% about 10 years after the event. As a whole, the effect of the viscoelastic relaxation becomes steady after 1000 years following the event. As time goes on, the effect of curvature decreases to 0.5% eventually.

5. *Application to the Tohoku-Oki M_w 9.0 Earthquake*

5.1. *GPS Data around the Tohoku-Oki M_w 9.0 Earthquake*

As an actual example, we estimate the post-seismic strain changes due to the Tohoku-Oki M_w 9.0 earthquake using our new Green's functions. The earthquake occurred near the east coast of Honshu Island on 11 March 2011, generated a huge tsunami, and caused huge loss of property and lives. The GPS

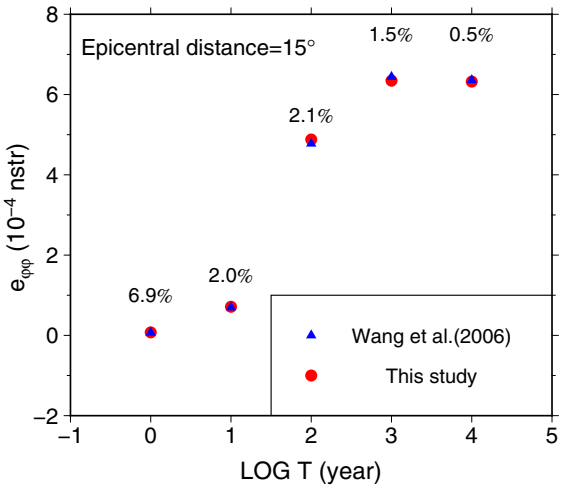

Figure 7
Comparison of our post-seismic strain changes caused by a point event (dip-slip angle of 45° and seismic depth of 10 km) with the results obtained from the half-space theory of Wang et al. (2006). The post-seismic strain changes occur at 1, 10, 100, 1000 and 10,000 years after the seismic event. The number above the red dots and blue triangle displays the curvature effect

network in Japan is of high quality and spatial resolution and provides valuable data to study the post-seismic processes that were associated with this earthquake (Fig. 8). We select the data of 298 continuous GPS stations in Fig. 8 that are evenly distributed around Honshu Island, with a date range between 11 March 2009 and 11 March 2017. The GPS data were processed by the Nevada Geodetic Laboratory (http://geodesy.unr.edu/) using GIPSY software in the global reference frame of IGS08. We remove the pre-earthquake velocities, and the annual and semiannual trends from the GPS data, using data from the 2 years before the event. The detailed process of GPS processing can be found in our previous study (Liu et al. 2017). We then divide the GPS data from the first 6 years after the earthquake into four periods (0–1.5, 1.5–3, 3–4.5 and 4.5–6 years after the earthquake). We show the velocities recorded by the GPS in Fig. 9.

5.2. *Post-seismic Strain Changes on Honshu Island Deduced from the GPS Data*

It is possible to calculate strain changes using GPS data. Some researchers approximate the surface of the Earth by a flat surface and use rectangular coordinates to calculate the strain changes; this approximation neglects the curvature of the Earth. Based on the above GPS data, in this study, we use the expressions in spherical coordinates developed by Savage et al. (2001) to calculate the strain changes induced by the Tohoku-Oki earthquake.

$$u_\theta = -\omega_\theta r_0 \cos\theta_0 \Delta\varphi + \omega_\phi r_0 + e_{\theta\varphi} r_0 \sin\theta_0 \Delta\varphi + r_0 e_{\theta\theta} \Delta\theta - \omega_r r_0 \sin\theta_0 \Delta\varphi, \tag{47}$$

$$u_\varphi = -\omega_\theta r_0 - \omega_\varphi r_0 \cos\theta_0 \Delta\varphi + e_{\varphi\varphi} r_0 \sin\theta_0 \Delta\theta + r_0 e_{\theta\varphi} \Delta\theta + r_0 \omega_r \Delta\theta. \tag{48}$$

Herein, θ corresponds to colatitude, φ to longitude, and r_0 to radial distance from the centre of the Earth. u_φ and u_θ represent the GPS-derived displacements in the east–west and south–north directions, respectively. $\Delta\varphi$, $\Delta\theta$ and Δr represent the distances of the GPS stations to the points that are chosen to calculate the strain changes. Given the displacements u_φ and u_θ at several stations, one can use the least-squares method to solve Eqs. (47, 48) and obtain the three components of the strain changes ($e_{\varphi\varphi}, e_{\theta\theta}, e_{\theta\varphi}$). Based on the three components of the strain, we can calculate the principal angle (α), the surface strain ($\varepsilon_{\text{area}}$) and the maximum and minimum principal strains ($\varepsilon_{1,2}$) using Eqs. (49–51).

$$\varepsilon_{1,2} = \frac{e_{\theta\theta} + e_{\varphi\varphi}}{2} \pm \sqrt{\left(\frac{e_{\theta\theta} - e_{\varphi\varphi}}{2}\right)^2 + \left(\frac{e_{\theta\varphi}}{2}\right)^2}, \tag{49}$$

$$\tan 2\alpha = \frac{e_{\theta\varphi}}{e_{\theta\theta} - e_{\varphi\varphi}}, \tag{50}$$

$$\varepsilon_{\text{area}} = e_{\theta\theta} + e_{\varphi\varphi}. \tag{51}$$

We show the surface strain changes on Honshu Island, including the directions and magnitudes of the principal strain changes, in Fig. 10, showing that significant strain changes [several thousand nstr (nano-strain)] occurred within 1.5 years after the earthquake. On the east coast of Honshu Island, near the earthquake, the surface shows a contraction state. However, most parts of Honshu Island are in a dilatation state. In addition, the strain changes in the northern part of the island are larger than those in the southern part, because the large ruptures were located in the north of the fault plane (Wei et al. 2012).

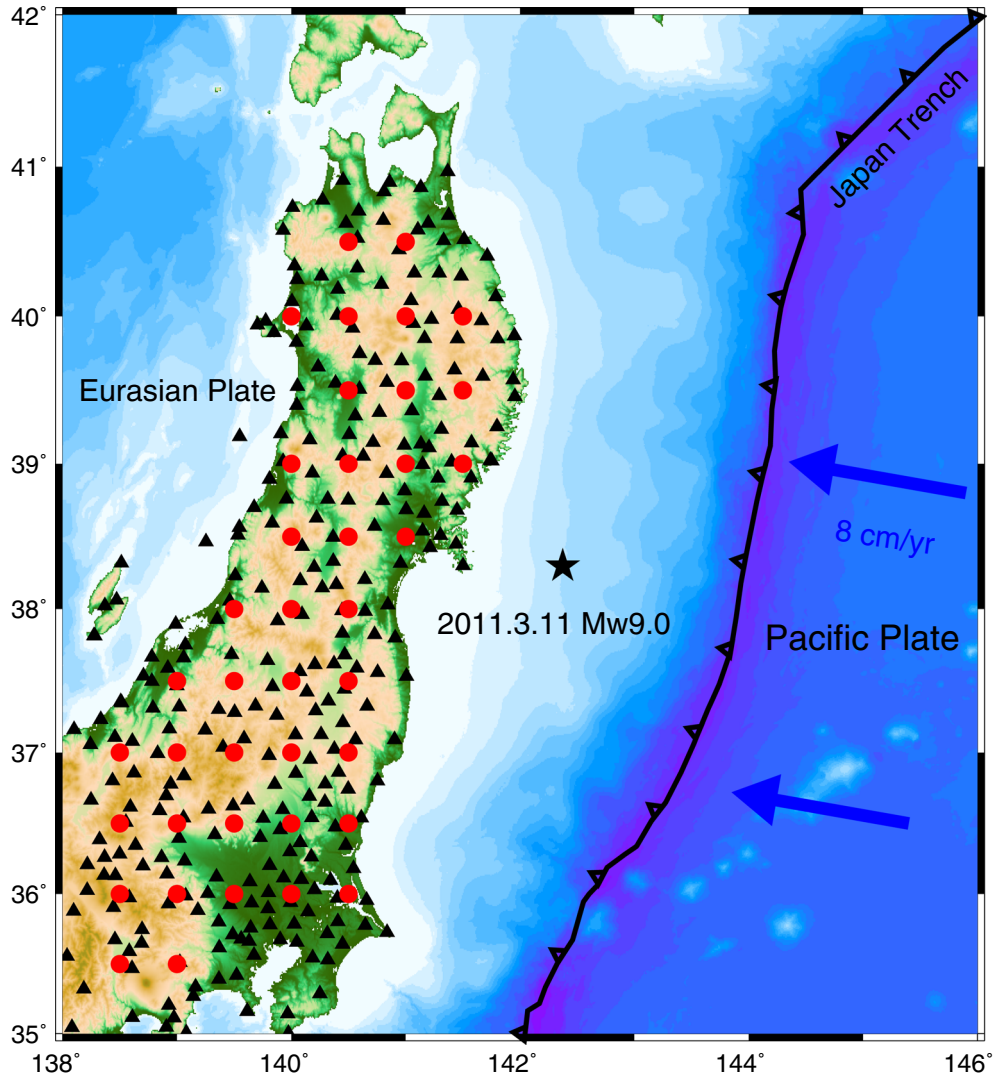

Figure 8
Configuration of the plate boundary and the locations of the GPS stations. The Pacific Plate is subducting westward beneath the Eurasian Plate with a velocity of 8 cm/year. The black triangles indicate the distribution of the 298 continuous GPS stations. The red circles indicate the points at which we deduce the post-seismic strain changes. The black star indicates the epicentre of the Tohoku-Oki M_w 9.0 earthquake

5.3. *Post-seismic Strain Changes on Honshu Island Calculated by Our Method*

In this subsection, we use our strain Green's functions to simulate the post-seismic strain changes induced by the Tohoku-Oki M_w 9.0 earthquake. In our calculations, we use the slip model proposed by Wei et al. (2012), which is inverted from both strong-motion waves and GPS observations. As in our previous study (Liu et al. 2017), we set the viscosity of the mantle and the thickness of the lithosphere to be about 6×10^{18} Pa s and 30 km, respectively. Finally, we obtain the post-seismic strain changes in the 6 years after the earthquake (Fig. 11).

Remember that our method is built on the point dislocation theory. Our Green's functions are calculated under the assumption that the size of the fault is negligible. However, real faults, such as the one that caused the Tohoku-Oki M_w 9.0 earthquake, always have finite size and dimensions. According to Sun

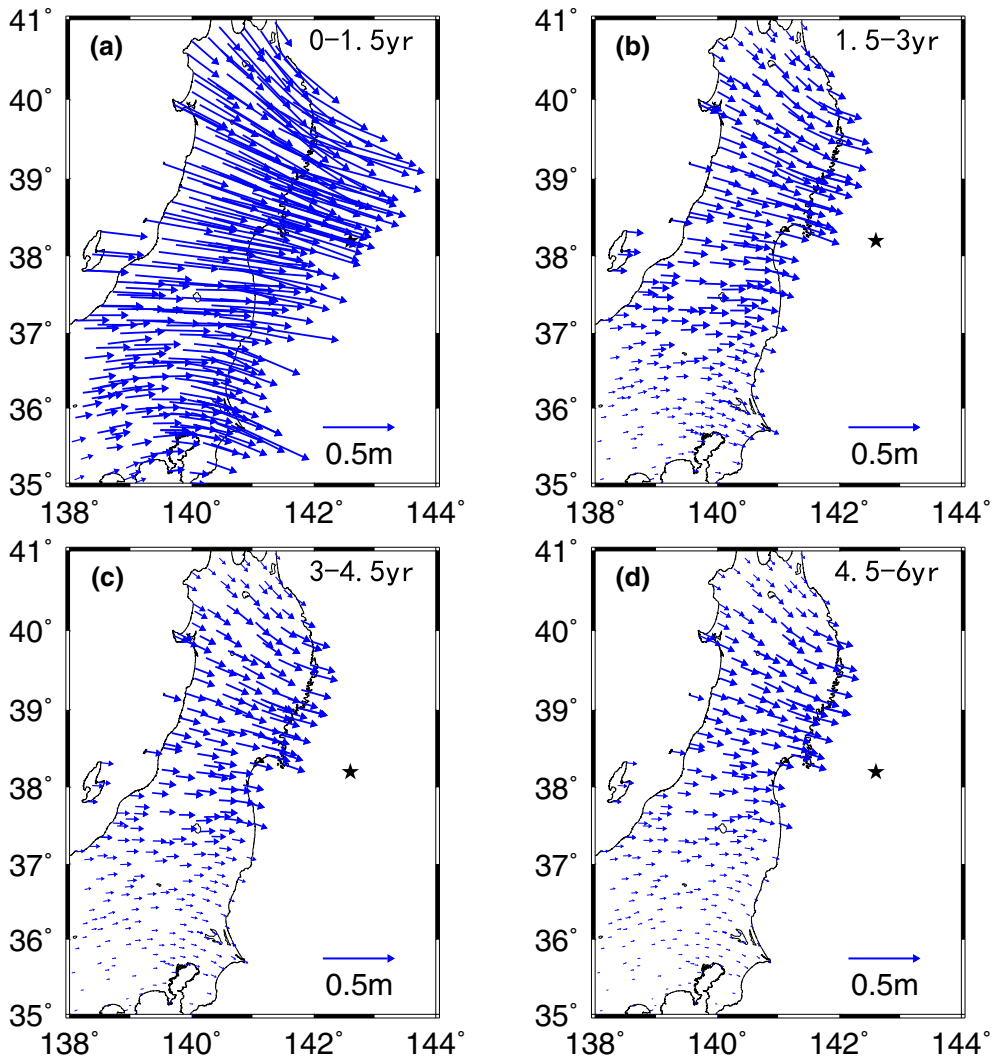

Figure 9
The GPS-derived post-seismic displacements on Honshu Island after the Tohoku-Oki M_w 9.0 earthquake

and Okubo (1998), the determination of whether the size of a fault is negligible is dependent on the relative position between the fault and the observation point. Without careful treatment of this distance, a calculation based on the point dislocation theory will produce large errors (Fu and Sun 2004). In this study, we regard a fault as a point source when the distance between the observation point and the centre of the fault is ten times larger than the longest side of the fault. Otherwise, we subdivide the subfault into smaller cells to ensure that they can be regarded as point sources, and the operational process becomes the same as Gao et al. (2017). Using this segment-summation scheme, we can calculate the near-field strain changes caused by the Tohoku-Oki M_w 9.0 earthquake with high accuracy.

After the Tohoku-Oki M_w 9.0 earthquake, many authors studied the mechanisms of the post-seismic deformations based on GPS data (Ozawa et al. 2012; Diao et al. 2014; Sun et al. 2014; Yamagiwa et al. 2015; Freed et al. 2017; Noda et al. 2018). They found that post-seismic deformation was primarily caused by after-slip over the initial 2 or 3 years after the event. The post-seismic deformations at longer

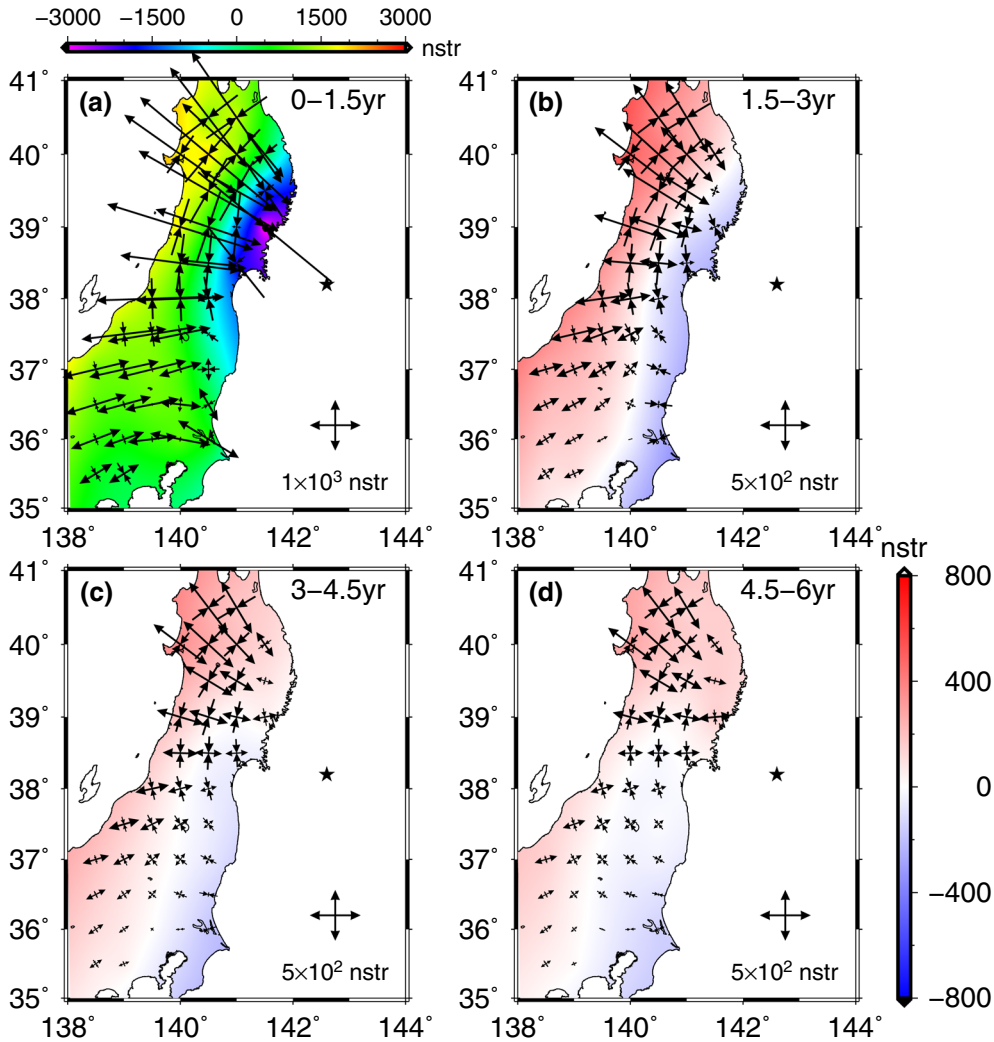

Figure 10
The post-seismic strain changes on Honshu Island deduced from the GPS data. The color indicates either contraction or dilatation fields. Orthogonal double arrows represent the horizontal directions and magnitudes of the principal strain changes

times following this great event result from viscoelastic relaxation. For this reason, we compare the strain changes deduced from the GPS displacement data (Fig. 10c, d) with the results obtained using our method (Fig. 11c, d) during 3–6 years after the main shock of the Tohoku-Oki M_w 9.0 earthquake, which was primarily caused by viscoelastic relaxation. In general, the two sets of results agree with each other.

The viscosity of the mantle plays an important role in simulations of post-seismic deformations. We change the viscosity of the mantle from 6×10^{18} to 6×10^{19} Pa s, and show the post-seismic strain changes within 6 years after the earthquake in Fig. 12. Comparing the strain changes in Figs. 11 and 12, we find that the amplitudes are significantly different between the two figures. The amplitudes of the deformations become much smaller when the viscosity becomes 10 times larger, although the patterns of the strain changes are overall consistent. Therefore, we can invert the viscosity of the mantle around the epicentre using the GPS data, the fault

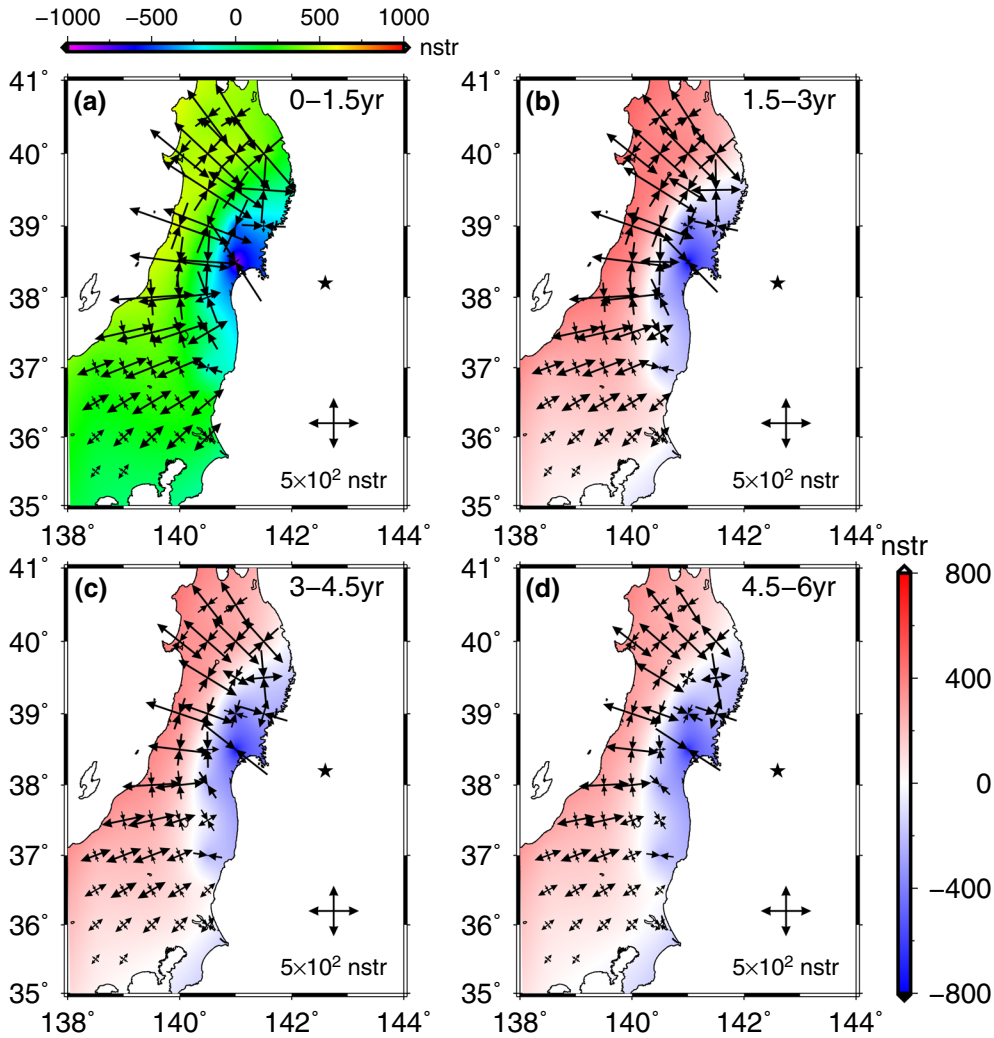

Figure 11
The post-seismic strain changes caused by the Tohoku-Oki M_w 9.0 earthquake on Honshu island of Japan, calculated using our new method. Symbols and colors as in Fig. 10

model of the great earthquake, as well as our post-seismic strain Green's functions.

5.4. *Far-Field Post-seismic Strain Changes Following the 2011 Tohoku-Oki M_w 9.0 Earthquake*

This section discusses the far-field post-seismic strain changes following the 2011 Tohoku-Oki M_w 9.0 earthquake. Zhao et al. (2018) extracted the post-seismic displacements in Northeastern China, South Korea and the Russian Far East following the earthquake. Northeast Asia is more than 1000 km away from the epicentre of the Tohoku-Oki M_w 9.0 earthquake. When we calculate the post-seismic strain changes induced by the earthquake in Northeast Asia using a dislocation theory, it is necessary to consider the curvature effect to obtain more accurate results.

We first divide the displacements presented by Zhao et al. (2018) over the first 4.5 years after the earthquake into three periods (0–1.5, 1.5–3.0 and 3.0–4.5 years after the earthquake). We find that the far-field post-seismic displacements decay more

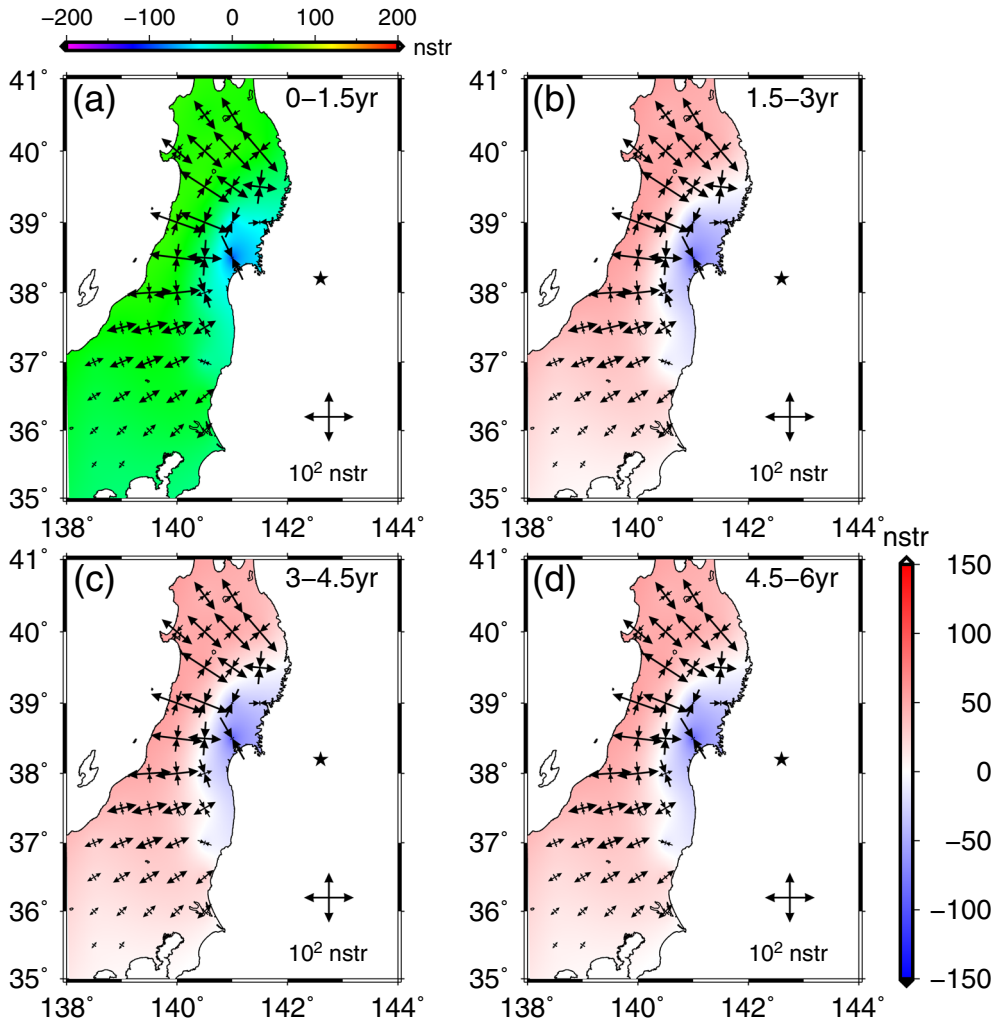

Figure 12
Post-seismic strain changes following the Tohoku-Oki M_w 9.0 earthquake calculated using our method when the viscosity of the mantle is 6×10^{19} Pa s. Symbols and colors as in Fig. 10

slowly than the near-field deformations do (Fig. 13). We then deduce the post-seismic strain changes over the above three periods using the least-squares method and GPS data and show them in Fig. 14. Limited by the sparse GPS stations used by Zhao et al. (2018), we calculate the strain changes at five points in the far field.

We also calculate the post-seismic strain changes following the Tohoku-Oki M_w 9.0 earthquake theoretically using the fault model of Wei et al. (2012) and our post-seismic Green's functions. In our calculation, we set the viscosity of the mantle to be 6×10^{18} Pa s, the same value as in the simulation in the near field (Fig. 11). From both the observations and simulations (Fig. 14), we find extensional strain changes in roughly east–west direction and compressional in roughly south–north direction in the far field. The observed and simulated strain changes agree with each other overall. The strain changes in the east–west direction are much larger than the corresponding ones in the south–north direction. This is because the Tohoku-Oki M_w 9.0 earthquake was a thrust-dominated event and the surface displacements along the dip of the seismic fault plane were significant, which has verified by GPS observations (Zhao et al. 2018). The GPS-deduced strain changes

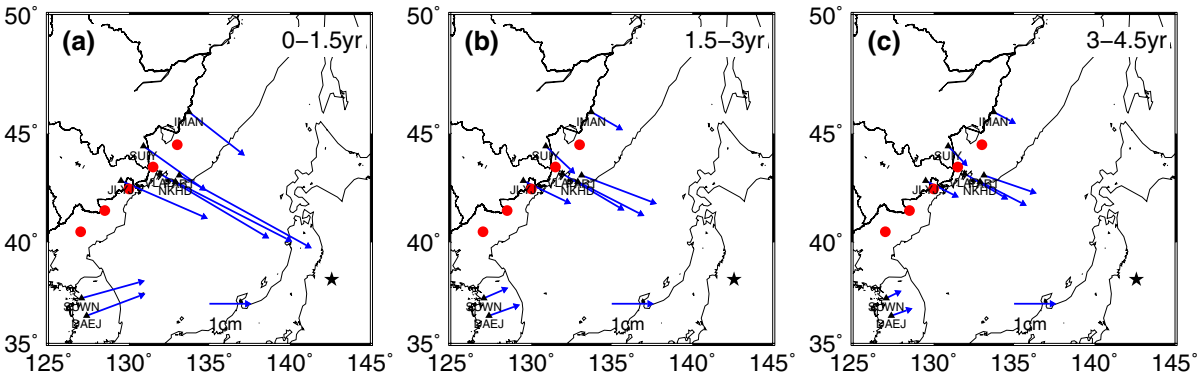

Figure 13
Post-seismic displacements in Northeastern China, South Korea and the Russian Far East. The red circles are the points at which the post-seismic strain changes are calculated. The black star indicates the epicentre of the Tohoku-Oki M_w 9.0 earthquake

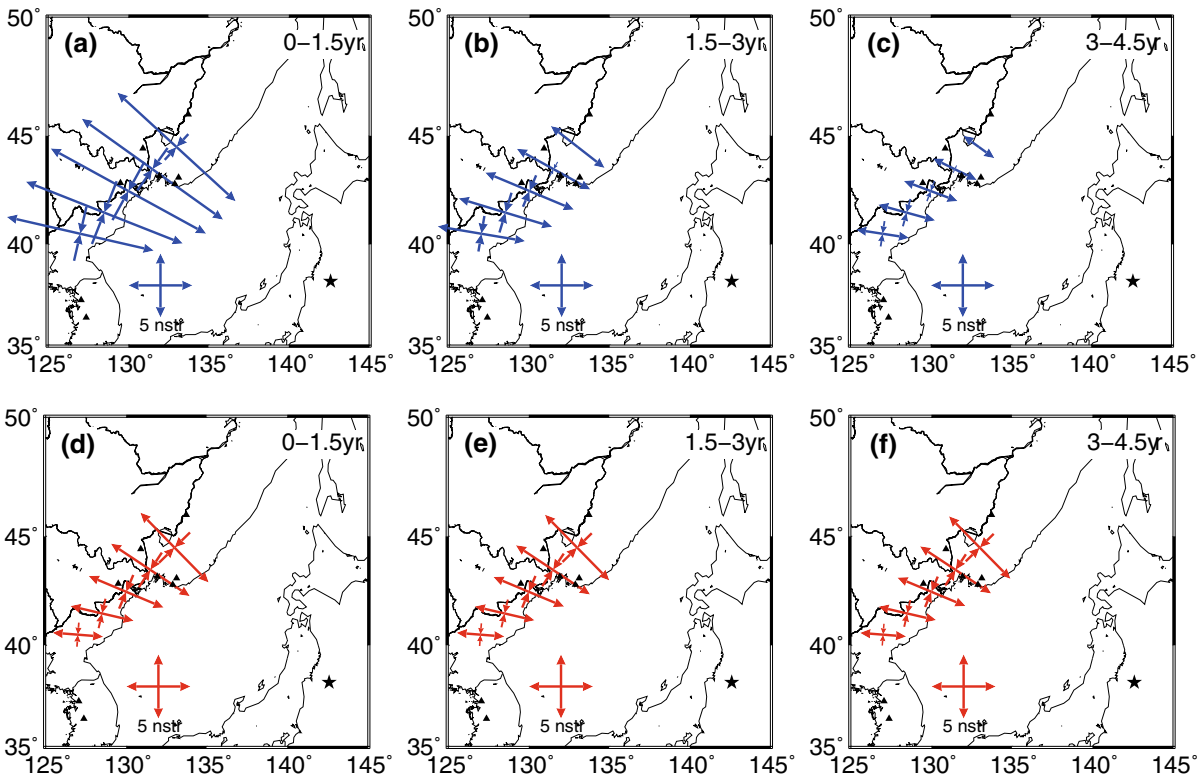

Figure 14
Far-field post-seismic strain changes following the Tohoku-Oki M_w 9.0 earthquake. **a–c** are the GPS-deduced post-seismic strain changes over the periods 0–1.5, 1.5–3.0 and 3.0–4.5 years after the earthquake, respectively. **d–f** are the corresponding theoretical strain changes calculated by our method

within the first 1.5 years after the earthquake (Fig. 14a) are much larger than those from the simulations (Fig. 14d). This is because the observations of this period include the effects of after-slips, which are large soon after the earthquake but decline quickly as time goes on (Liu et al. 2017).

Next, we compare the computed and observed strain changes in both the near and far field to display the extent to which the theoretical computations agree with the observed strain changes. We first calculate the epicentral distances of each point to deduce the post-seismic strain changes. We then divide these points into seven groups according to epicentral distances (100–150 km, 150–200 km, 200–250 km, 250–300 km, 300–350 km, 350–400 km and > 400 km). Next, we calculate the average error between observations and expectations in each group using Eq. (52). Note that we focused on the surface strains ($\varepsilon_{\text{area}}$) between 3.0 and 4.5 years after the great earthquake, because the deformation in this period is primarily caused by viscoelastic relaxation (Liu et al. 2017; Yamagiwa et al. 2015).

$$\varepsilon = \frac{|\bar{e}_{\text{obs}} - \bar{e}_{\text{cal}}|}{|\bar{e}_{\text{obs}}|}. \tag{52}$$

Herein, $\bar{e}_{\text{obs}}$ and $\bar{e}_{\text{cal}}$ represent the GPS-deduced post-seismic strain changes and calculations, respectively. The relative errors are shown in Table 2. We find that the relative error is large in the near field. This is because the near-field deformation is sensitive to the slip model. The details of the distribution using the slip model can significantly affect the near-field deformation (Zhou et al. 2012). As the epicentral distance increases, the relative errors decrease, showing the advantages of our method for research in the far field.

Table 2

The relative error of the calculated and observed strain changes over the period from 3.0–4.5 years after the Tohoku-Oki M_w 9.0 earthquake

Epicentral distance (km)	Relative error (%)
100–150	1400.51
150–200	147.61
200–250	150.78
250–300	99.72
300–350	67.07
350–400	16.53
> 400	9.98

6. Conclusions

We present a set of Green's functions for the post-seismic surface strain changes for four independent point events (strike-slip, dip-slip, and horizontal and vertical tensile sources) in a realistic spherical Earth model. Using these Green's functions, we can calculate the post-seismic strain changes caused by an arbitrary earthquake at an arbitrary time afterwards. The agreement between the co-seismic strain changes obtained using our method and those obtained using the method of Sun et al. (2006) yields an elastic response, and the agreement between the post-seismic strain changes in the near field calculated by our method and the half-space dislocation theory (Wang et al. 2006) yields a viscoelastic response. When the epicentral distances are smaller than 15°, the effects of the curvature are less than 5% in total. However, with an increase in the epicentral distance, the effect of the curvature in both co- and post-seismic strain changes increases rapidly. Finally, we calculate the post-seismic strain changes after the Tohoku-Oki M_{w} 9.0 earthquake using our strain Green's functions. Our calculated results agree with the GPS-derived strain changes as a whole. As the epicentral distance increases, the relative errors between the GPS-deduced and theoretically calculated strain changes over the period from 3.0 to 4.5 years after the earthquake diminishes rapidly (Table 2), confirming the advantages of our strain Green's functions for research in the far field.

Acknowledgements

We thank two anonymous reviewers for their helpful comments and suggestions. We thank Dr. Yoshiyuki Tanaka at Earthquake Research Institute, the University of Tokyo for providing us with his computer codes, which helped us to establish the Green's functions for post-seismic strain changes. The Green's functions are available in Table 1. This work was financially supported by the National Science Foundation of China (41574071; 41874003; 41331066) and the Basic Research Projects of Institute of Earthquake Science, China Earthquake Administration (2016IES010204).

Appendices

Appendix 1: Explicit Expressions for the Homogeneous Terms

According to Takeuchi and Saito (1972), one can obtain the numerical solution of Eqs. (6) and (7) when excluding excitation terms.

The explicit expressions for the homogeneous terms are specifically written as

$$\frac{\mathrm{d}\tilde{y}_1}{\mathrm{d}r} = \frac{1}{\lambda+2\mu}\left(\tilde{y}_2 - \frac{\lambda}{r}[2\tilde{y}_1 - n(n+1)\tilde{y}_3]\right), \tag{53}$$

$$\begin{aligned}\frac{\mathrm{d}\tilde{y}_2}{\mathrm{d}r} =& -s^2\rho\tilde{y}_1 + \frac{2}{r}\left(\lambda\frac{d\tilde{y}_1}{\mathrm{d}r} - \tilde{y}_2\right)\\ &+ \frac{1}{r}\left(\frac{2(\lambda-\mu)}{r} - \rho g\right)[2\tilde{y}_1 - n(n+1)\tilde{y}_3]\\ &+ \frac{n(n+1)}{r}\tilde{y}_4 - \rho\left(\tilde{y}_6 - \frac{n+1}{r}\tilde{y}_5 + \frac{2g}{r}\tilde{y}_1\right),\end{aligned} \tag{54}$$

$$\frac{\mathrm{d}\tilde{y}_3}{\mathrm{d}r} = \frac{1}{\mu}\tilde{y}_4 + \frac{1}{r}(\tilde{y}_3 - \tilde{y}_1), \tag{55}$$

$$\begin{aligned}\frac{\mathrm{d}\tilde{y}_4}{\mathrm{d}r} =& -s^2\rho\tilde{y}_3 - \frac{\lambda}{r}\frac{\mathrm{d}\tilde{y}_1}{\mathrm{d}r} - \frac{\lambda+2\mu}{r_2}[2\tilde{y}_1 - n(n+1)\tilde{y}_3]\\ &+ \frac{2\mu}{r_2}(\tilde{y}_1 - \tilde{y}_3) - \frac{3}{r}\tilde{y}_4 - \frac{\rho}{r}(\tilde{y}_5 - g\tilde{y}_1),\end{aligned} \tag{56}$$

$$\frac{\mathrm{d}\tilde{y}_5}{\mathrm{d}r} = \tilde{y}_6 + 4\pi G\rho\tilde{y}_1 - \frac{n+1}{r}\tilde{y}_5, \tag{57}$$

$$\begin{aligned}\frac{\mathrm{d}\tilde{y}_6}{\mathrm{d}r} =& \frac{n-1}{r}(\tilde{y}_6 + 4\pi G\rho\tilde{y}_1)\\ &+ \frac{4\pi G\rho}{r}[2\tilde{y}_1 - n(n+1)\tilde{y}_3],\end{aligned} \tag{58}$$

$$\frac{\mathrm{d}\tilde{y}_1^{\mathrm{T}}}{\mathrm{d}r} = \frac{1}{r}\tilde{y}_1^{\mathrm{T}} + \frac{1}{\mu}\tilde{y}_2^{\mathrm{T}}, \tag{59}$$

$$\frac{\mathrm{d}\tilde{y}_2^{\mathrm{T}}}{\mathrm{d}r} = \left[\frac{(n-1)(n+2)\mu}{r^2} + s^2\rho\right]\tilde{y}_1^{\mathrm{T}} - \frac{3}{r}\tilde{y}_2^{\mathrm{T}}, \tag{60}$$

where $\lambda(s) = \frac{\lambda s + \mu K/\eta}{s+\mu/\eta}$, $\mu(s) = \frac{\mu s}{s+\mu/\eta}$, $K = \lambda + \frac{2}{3}\mu$, based on the Laplace transform of Maxwell's constitutive equation (Peltier 1974); and $g = |\boldsymbol{g}(\boldsymbol{r})|$ denotes the magnitude of the gravity (Takeuchi and Saito 1972).

Appendix 2: The Solution of the Differential Equation

According to Tanaka et al. (2006, 2007), the expressions for F_v^i (i = 1,…,4), F_u^i (i = 1,…,4) and F_t^i (i = 1, 2) can be expressed as follows:

$$\begin{aligned}F_u^1(t;n) =& -\frac{1}{2\pi i}\frac{G}{g_0 a}\\ &\oint\left[\frac{3\lambda(r_s,s)+2\mu(r_s,s)}{\lambda(r_s,s)+2\mu(r_s,s)}\frac{1}{r_s}X^{\mathrm{Press}}(r_s,s;n)\right.\\ &\left.+\frac{\lambda(r_s,s)}{\lambda(r_s,s)+2\mu(r_s,s)}x_2^{\mathrm{Press}}(r_s,s;n)\right]\frac{\mathrm{e}^{st}}{s}\mathrm{d}s,\end{aligned} \tag{61}$$

$$F_u^2(t;n) = -\frac{1}{2\pi i}\frac{G}{g_0 a}\oint x_2^{\mathrm{Press}}(r_s,s;n)\frac{\mathrm{e}^{st}}{s}\mathrm{d}s, \tag{62}$$

$$F_u^3(t;n) = -\frac{1}{2\pi i}\frac{G}{g_0 a}\oint x_3^{\mathrm{Press}}(r_s,s;n)\frac{\mathrm{e}^{st}}{s}\mathrm{d}s, \tag{63}$$

$$F_u^4(t;n) = -\frac{1}{2\pi i}\frac{G}{g_0 a}\oint x_4^{\mathrm{Press}}(r_s,s;n)\frac{\mathrm{e}^{st}}{s}\mathrm{d}s, \tag{64}$$

$$\begin{aligned}F_v^1(t;n) =& -\frac{1}{2\pi i}\frac{G}{g_0 a}\\ &\oint\left[\frac{3\lambda(r_s,s)+2\mu(r_s,s)}{\lambda(r_s,s)+2\mu(r_s,s)}\frac{1}{r_s}X^{\mathrm{Shear}}(r_s,s;n)\right.\\ &\left.+\frac{\lambda(r_s,s)}{\lambda(r_s,s)+2\mu(r_s,s)}x_2^{\mathrm{Shear}}(r_s,s;n)\right]\frac{\mathrm{e}^{st}}{s}\mathrm{d}s,\end{aligned} \tag{65}$$

$$F_v^2(t;n) = -\frac{1}{2\pi i}\frac{G}{g_0 a}\oint x_2^{\mathrm{Shear}}(r_s,s;n)\frac{\mathrm{e}^{st}}{s}\mathrm{d}s, \tag{66}$$

$$F_v^3(t;n) = -\frac{1}{2\pi i}\frac{G}{g_0 a}\oint x_3^{\mathrm{Shear}}(r_s,s;n)\frac{\mathrm{e}^{st}}{s}\mathrm{d}s, \tag{67}$$

$$F_v^4(t;n) = -\frac{1}{2\pi i}\frac{G}{g_0 a}\oint x_4^{\mathrm{Shear}}(r_s,s;n)\frac{\mathrm{e}^{st}}{s}\mathrm{d}s, \tag{68}$$

$$F_t^1(t;n) = \frac{1}{2\pi i}\frac{G}{g_0 a}\oint x_1^{\mathrm{T}}(r_s,s;n)\frac{\mathrm{e}^{st}}{s}\mathrm{d}s, \tag{69}$$

$$F_t^2(t;n) = -\frac{1}{2\pi i}\frac{G}{g_0 a}\oint x_2^{\mathrm{T}}(r_s,s;n)\frac{\mathrm{e}^{st}}{s}\mathrm{d}s. \tag{70}$$

In the above equations, the relationship between X, x_1 and x_3 can be found in Okubo (1993) as

$$X^{\mathrm{Press}} = 2x_1^{\mathrm{Press}} - n(n+1)x_3^{\mathrm{Press}}, \tag{71}$$

$$X^{\mathrm{Shear}} = 2x_1^{\mathrm{Shear}} - n(n+1)x_3^{\mathrm{Shear}}. \tag{72}$$

References

Araya, A., Takamori, A., Morii, W., Hayakawa, H., Uchiyama, T., & Ohashi, M. (2010). Analyses of far-field coseismic crustal deformation observed by a new laser distance measurement system. *Geophysical Journal International, 181,* 127–140.

Araya, A., Takamori, A., Morii, W., Miyo, K., Ohashi, M., & Hayama, K. (2017). Design and operation of a 1500-m laser strainmeter installed at an underground site in Kamioka, Japan. *Earth Planets Space, 69,* 77.

Chinnery, M. A. (1961). The deformation of ground around surface faults. *Bulletin of the Seismological Society of America, 51,* 355–372.

Chinnery, M. A. (1963). The stress changes that accompany strike-slip faulting. *Bulletin of the Seismological Society of America, 53,* 921–932.

Diao, F., Xiong, X., Wang, R., Zheng, Y., Walter, T. R., Weng, H., et al. (2014). Overlapping post-seismic deformation processes: Afterslip and viscoelastic relaxation following the 2011 M_w 9.0 Tohoku (Japan) earthquake. *Geophysical Journal International, 196,* 218–229.

Dong, J., Sun, W., Zhou, X., & Wang, R. (2014). Effects of earth's layered structure, gravity and curvature on coseismic deformation. *Geophysical Journal International, 199,* 1442–1451.

Dong, J., Sun, W., Zhou, X., & Wang, R. (2016). An analytical approach to estimate curvature effect of coseismic deformations. *Geophysical Journal International, 206,* 1327–1339.

Dziewonski, A. M., & Anderson, A. (1981). Preliminary reference earth model. *Physics of the Earth and Planetary Interiors, 25,* 297–356.

Fang, M., & Hager, B. H. (1994). A singularity free approach to post glacial rebound calculations. *Geophysical Research Letters, 21,* 2131–2134.

Freed, A. M., Hashima, A., Becker, T. W., Okaya, D. A., Sato, H., & Hatanaka, Y. (2017). Resolving depth-dependent subduction zone viscosity and afterslip from postseismic displacements following the 2011 Tohoku-oki, Japan earthquake. *Earth and Planetary Science Letters, 459,* 279–290.

Fu, G., & Sun, W. (2004). Effects of spatial distribution of fault slip on calculating co-seismic displacement: case studies of the Chi-Chi earthquake (M_w 7.6) and the Kunlun earthquake (M_w 7.8). *Geophysical Research Letters, 31,* 177–178.

Fukahata, Y., & Matsu'ura, M. (2005). General expressions for internal deformation fields due to a dislocation source in a multilayered elastic halfspace. *Geophysical Journal International, 161,* 507–521.

Fukahata, Y., & Matsu'ura, M. (2006). Quasi-static internal deformation due to a dislocation source in a multilayered elastic/viscoelastic half-space and an equivalence theorem. *Geophysical Journal International, 166,* 418–434.

Gao, S., Fu, G., Liu, T., & Zhang, G. (2017). A new code for calculating post-seismic displacements as well as geoid and gravity changes on a layered visco-elastic spherical earth. *Pure and Applied Geophysics, 174,* 1167–1180.

Hashima, A., Fukahata, Y., Hashimoto, C., & Matsu'ura, M. (2014). Quasi-static strain and stress fields due to a moment tensor in elastic–viscoelastic layered half-space. *Pure and Applied Geophysics, 171,* 1669–1693.

Hashima, A., Takada, Y., Fukahata, Y., & Matsu'ura, M. (2008). General expressions for internal deformation due to a moment tensor in an elastic/viscoelastic multilayered half-space. *Geophysical Journal International, 175,* 992–1012.

Lee, E. H. (1955). Stress analysis in visco-elastic bodies. *Quarterly of Applied Mathematics, 13,* 183–190.

Liu, T., Fu, G., Zhou, X., & Su, X. (2017). Mechanism of post-seismic deformations following the 2011 Tohoku-Oki M_w 9.0 earthquake and general structure of lithosphere around the sources. *Chinese Journal of Geophysics, 60,* 3406–3417. **(in Chinese)**.

Maruyama, T. (1964). Statical elastic dislocations in an infinite and semi-infinite medium. *Bulletin of the Earthquake Research Institute, University of Tokyo, 42,* 289–368.

Noda, A., Takahama, T., Kawasato, T., & Matsu'ura, M. (2018). Interpretation of offshore crustal movements following the 2011 Tohoku-oki earthquake by the combined effect of afterslip and viscoelastic stress relaxation. *Pure and Applied Geophysics, 175,* 559–572.

Ohzono, M., Yabe, Y., Iinuma, T., Yusaku, O., Miura, S., & Tachibana, K. (2012). Strain anomalies induced by the 2011 Tohoku Earthquake (M_w, 9.0) as observed by a dense GPS network in northeastern Japan. *Earth Planets Space, 64,* 1231–1238.

Okada, Y. (1985). Surface deformation due to shear and tensile faults in a half-space. *Bulletin of the Seismological Society of America, 75,* 1135–1154.

Okubo, S. (1991). Potential and gravity changes raised by point dislocations. *Geophysical Journal International, 105,* 573–586.

Okubo, S. (1992). Potential and gravity changes due to shear and tensile faults in a half-space. *Journal of Geophysical Research, 97,* 7137–7144.

Okubo, S. (1993). Reciprocity theorem to compute the static deformation due to a point dislocation buried in a spherically symmetric earth. *Geophysical Journal International, 115,* 921–928.

Ozawa, S., Nishimura, T., Munekata, H., Suito, H., Kobayashi, T., Tobita, M., et al. (2012). Preceding, coseismic, and postseismic slips of the 2011 Tohoku earthquake, Japan. *Journal of Geophysical Research, 117,* B07404. https://doi.org/10.1029/2011JB009120.

Ozawa, S., Nishimura, T., Suito, H., Kobayashi, T., Tobita, M., & Imakiire, T. (2011). Coseismic and postseismic slip of the 2011 magnitude-9 Tohoku-oki earthquake. *Nature, 475,* 373–376.

Peltier, W. R. (1974). The impulse response of a Maxwell Earth. *Reviews of Geophysics, 12,* 649–669.

Piersanti, A., Spada, G., Sabadini, R., & Bonafede, M. (1995). Global postseismic deformation. *Geophysical Journal International, 120,* 544–566.

Pollitz, F. F. (1997). Gravitational viscoelastic postseismic relaxation on a layered spherical Earth. *Journal of Geophysical Research, 102,* 17921–17941.

Radok, J. R. M. (1957). Visco-elastic stress analysis. *Quarterly of Applied Mathematics, 15,* 198–202.

Saito, M. (1967). Excitation of free oscillations and surface waves by a point source in a vertically heterogeneous earth. *Journal of Geophysical Research, 72,* 3689–3699.

Savage, J. C., Gan, W., & Svarc, J. L. (2001). Strain accumulation and rotation in the Eastern California Shear Zone. *Journal of Geophysical Research, 106,* 21995–22007.

Savage, J. C., Prescott, W. H., & Gu, G. (1986). Strain accumulation in southern California, 1973–1984. *Journal of Geophysical Research, 91,* 7455–7473.

Steketee, J. A. (1958). On Volterra's dislocations in a semi-infinite elastic medium. *Canadian Journal of Physics, 36,* 192–205.

Sun, W., & Okubo, S. (1998). Surface potential and gravity changes due to internal dislocations in a spherical earth -II. Application to a finite fault. *Geophysical Journal International, 132,* 79–88.

Sun, W., & Okubo, S. (2002). Effects of earth's spherical curvature and radial heterogeneity in dislocation studies—for a point dislocation. *Geophysical Research Letters, 29,* 46–1–46-4.

Sun, W., Okubo, S., & Fu, G. (2006). Green's functions of co-seismic strain changes and investigation of effect of earth's spherical curvature and radial heterogeneity. *Geophysical Journal International, 167,* 1273–1291.

Sun, W., Okubo, S., Fu, G., & Araya, A. (2009). General formulations of global co-seismic deformations caused by an arbitrary dislocation in a spherically symmetric earth model—applicable to deformed earth surface and space-fixed point. *Geophysical Journal International, 177,* 817–833.

Sun, W., Okubo, S., & Vaníček, P. (1996). Global displacements caused by point dislocations in a realistic Earth model. *Journal of Geophysical Research, 101,* 8561–8578.

Sun, T., Wang, K., Iinuma, T., Hino, R., He, J., Fujimoto, H., et al. (2014). Prevalence of viscoelastic relaxation after the 2011 Tohoku-oki earthquake. *Nature, 514*(7520), 84–87.

Takagi, Y., & Okubo, S. (2017). Internal deformation caused by a point dislocation in a uniform elastic sphere. *Geophysical Journal International, 208,* 973–991.

Takahashi, H. (2011). Static strain and stress changes in eastern Japan due to the 2011 off the Pacific coast of Tohoku Earthquake, as derived from GPS data. *Earth Planets Space, 63,* 741–744.

Takeuchi, H., & Saito, M. (1972). Seismic surface waves. *Methods in Computational Physics Advances in Research & Applications, 11,* 217–295.

Tanaka, T., Okuno, J., & Okubo, S. (2006). A new method for the computation of global viscoelastic post-seismic deformation in a realistic earth model (I)—vertical displacement and gravity variation. *Geophysical Journal International, 164,* 273–289.

Tanaka, T., Okuno, J., & Okubo, S. (2007). A new method for the computation of global viscoelastic post-seismic deformation in a realistic earth model (II)—Horizontal displacement. *Geophysical Journal International, 170,* 1031–1052.

Tang, H., & Sun, W. (2017). Asymptotic expressions for changes in the surface co-seismic strain on a homogeneous sphere. *Geophysical Journal International, 209,* 202–225.

Tape, C., Musé, P., Simons, M., Dong, D., & Webb, F. (2009). Multiscale estimation of GPS velocity fields. *Geophysical Journal International, 179,* 945–971.

Vermeersen, L. L. A., & Sabadini, R. (1997). A new class of stratified viscoelastic models by analytical techniques. *Geophysical Journal International, 129,* 531–570.

Wang, H. (1999). Surface vertical displacements, potential perturbations and gravity changes of a viscoelastic earth model induced by internal point dislocations. *Geophysical Journal International, 137,* 429–440.

Wang, R., Lorenzo-Martin, F., & Roth, F. (2003). Computation of deformation induced by earthquakes in a multi-layered elastic crust—FORTRAN programs EDGRN/EDCMP. *Computer & Geosciences, 29,* 195–207.

Wang, R., Lorenzo-Martin, F., & Roth, F. (2006). PSGRN/PSCMP—a new code for calculating co- and post-seismic deformation, geoid and gravity changes based on the viscoelastic-gravitational dislocation theory. *Computer & Geosciences, 32,* 527–541.

Wei, S., Graves, R., Helmberger, D., Avouac, J. P., & Jiang, J. (2012). Sources of shaking and flooding during the Tohoku-Oki earthquake: a mixture of rupture styles. *Earth and Planetary Science Letters, 333–334,* 91–100.

Yamagiwa, S., Miyazaki, S., Hirahara, K., & Fukahata, Y. (2015). Afterslip and viscoelastic relaxation following the 2011 Tohoku-oki earthquake (M_w 9.0) inferred from inland GPS and seafloor GPS/acoustic data. *Geophysical Research Letters, 42,* 66–73.

Zhao, Q., Fu, G., Wu, W., Liu, T., Su, L., Su, X., et al. (2018). Spatial-temporal evolution and corresponding mechanism of the far-field post-seismic displacements following the 2011 M_w 9. 0 Tohoku earthquake. *Geophysical Journal International, 214,* 1774–1782.

Zhou, X., Cambiotti, G., Sun, W., & Sabadini, R. (2014). The coseismic slip distribution of a shallow subduction fault constrained by prior information: the example of 2011 Tohoku (M_w 9.0) megathrust earthquake. *Geophysical Journal International, 199,* 981–995.

Zhou, X., Sun, W., Zhao, B., Fu, G., Dong, J. & Nie, Z. (2012). Geodetic observations detecting coseismic displacements and gravity changes caused by the M_w = 9.0 Tohoku-Oki earthquake. *Journal of Geophysical Research*, *117*, https://doi.org/10.1029/2011jb008849.

(Received June 6, 2018, revised November 8, 2018, accepted November 17, 2018, Published online November 27, 2018)